




















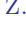







A Hyperactive FRB Pinpointed in an SMC-Like Satellite Host Galaxy

M. BHARDWAJ[†] ¹, M. P. SNELDERS[†] ^{2,3}, J. W. T. HESSELS ^{4,5,2,3}, A. GIL DE PAZ ^{6,7}, S. BHANDARI ⁸,
B. MARCOTE ^{9,2}, A. KIRICHENKO ¹⁰, O. S. OULD-BOUKATTINE ^{2,3}, F. KIRSTEN ^{11,2},
E. K. BEMPONG-MANFUL ^{12,13}, V. BEZRUKOV ¹⁴, J. D. BRAY ¹², S. BUTTACCIO ^{15,16}, A. CORONGIU ¹⁷,
R. FEILER ¹⁸, M. P. GAWROŃSKI ^{18,3}, M. GIROLETTI ¹⁵, D. M. HEWITT ³, M. LINDQVIST ¹¹, G. MACCAFERRI ¹⁵,
A. MOROIANU ³, K. NIMMO ¹⁹, Z. PARAGI ⁹, W. PUCHALSKA ¹⁸, N. WANG ²⁰, D. WILLIAMS-BALDWIN ¹² AND
J.P. YUAN ²⁰

- ¹McWilliams Center for Cosmology & Astrophysics, Department of Physics, Carnegie Mellon University, Pittsburgh, PA 15213, USA
²ASTRON, Netherlands Institute for Radio Astronomy, Oude Hoogeveensedijk 4, 7991 PD Dwingeloo, The Netherlands
³Anton Pannekoek Institute for Astronomy, University of Amsterdam, Science Park 904, 1098 XH, Amsterdam, The Netherlands
⁴Department of Physics, McGill University, 3600 rue University, Montréal, QC H3A 2T8, Canada
⁵Trottier Space Institute, McGill University, 3550 rue University, Montréal, QC H3A 2A7, Canada
⁶Departamento de Física de la Tierra y Astrofísica, Facultad de CC. Físicas, Universidad Complutense de Madrid, E-28040, Madrid, Spain
⁷Instituto de Física de Partículas y del Cosmos IPARCOS, Facultad de CC. Físicas, Universidad Complutense de Madrid, E-28040 Madrid, Spain
⁸SKA Observatory (SKAO), Science Operations Centre, CSIRO ARRC, Kensington WA 6151, Australia
⁹Joint Institute for VLBI ERIC, Oude Hoogeveensedijk 4, 7991 PD Dwingeloo, The Netherlands
¹⁰Instituto de Astronomía, Universidad Nacional Autónoma de México, Apdo. Postal 877, Ensenada, Baja California 22800, México
¹¹Department of Space, Earth and Environment, Chalmers University of Technology, Onsala Space Observatory, 439 92, Onsala, Sweden
¹²Jodrell Bank Centre for Astrophysics, Dept. of Physics & Astronomy, University of Manchester, Manchester M13 9PL, UK
¹³School of Physics, University of Bristol, Tyndall Avenue, Bristol BS8 1TL, UK
¹⁴Engineering Research Institute Ventspils International Radio Astronomy Centre (ERI VIRAC) of Ventspils University of Applied Sciences, Inženieru street 101, Ventspils, LV-3601, Latvia
¹⁵INAF-Istituto di Radioastronomia, Via Gobetti 101, 40129, Bologna, Italy
¹⁶INAF-Osservatorio Astrofisico di Catania, via Santa Sofia 78, I-95123, Catania, Italy
¹⁷INAF-Osservatorio Astronomico di Cagliari, via della Scienza 5, I-09047, Selargius (CA), Italy
¹⁸Institute of Astronomy, Faculty of Physics, Astronomy and Informatics, Nicolaus Copernicus University, Grudziadzka 5, PL-87-100 Toruń, Poland
¹⁹MIT Kavli Institute for Astrophysics and Space Research, Massachusetts Institute of Technology, 77 Massachusetts Ave, Cambridge, MA 02139, USA
²⁰Xinjiang Astronomical Observatory, CAS, 150 Science 1-Street, Urumqi, Xinjiang 830011, China

ABSTRACT

Precise localizations of fast radio bursts (FRBs) are essential for uncovering their host galaxies and immediate environments. We present the milliarcsecond-precision European VLBI Network (EVN) localization of FRB 20240114A, a hyper-active repeating FRB, achieving $\lesssim 90 \times 30$ mas ($1\text{-}\sigma$) accuracy. This precision places the burst 0.5 kpc from the nucleus of its low-metallicity star-forming dwarf host at a spectroscopic redshift of $z = 0.1300$. Our Gran Telescopio CANARIAS (GTC) spectroscopic follow-up reveals that the dwarf FRB host is gravitationally bound to a more massive, star-forming spiral galaxy. This establishes the first known instance of an FRB residing in a satellite galaxy within a larger galactic system. This configuration, analogous to the Small Magellanic Cloud orbiting the Milky Way (but at a lower overall mass scale), expands the known diversity of FRB host environments and offers important insights for interpreting seemingly “hostless” or highly offset FRBs. Furthermore, our detailed dispersion measure (DM) budget analysis indicates that the dominant contribution to FRB 20240114A’s DM likely originates from the foreground halo of the central galaxy. This finding

addresses the anomalously high DM observed for this FRB and underscores the significant role of intervening foreground structures in shaping observed FRB DMs, which is important for accurate FRB-based cosmological measurements. Our results highlight the importance of deep, high-resolution optical/infrared observations (e.g., with *Hubble* or *James Webb Space Telescopes*) to fully leverage our precise radio localization and probe the immediate astrophysical birthplaces of FRB progenitors within these complex galactic systems.

Keywords: Companion galaxies (290) — Dwarf galaxies (416) — Very long baseline interferometry (1769) — Radio bursts (1339) — Radio transient sources (2008)

1. INTRODUCTION

Fast radio bursts (FRBs) are brief flashes of radio waves originating from extragalactic distances (Lorimer et al. 2007). Given the observed energetics and timescales of FRBs they must come from compact objects (see, e.g., Petroff et al. 2022, for a review), but their exact origin(s) and emission mechanism(s) remain unclear. A small fraction ($\sim 2\%$) of the FRB population has been observed to repeat (e.g., Spitler et al. 2016; CHIME/FRB Collaboration et al. 2023), which shows that at least a part of the population requires a longer-lived central engine. The magnetically powered neutron stars known as ‘magnetars’ are a popular explanation for the FRB phenomenon — both because of an energetic FRB-like event from a known Galactic magnetar, SGR 1935+2154 (Bochenek et al. 2020; CHIME/FRB Collaboration et al. 2020), and the large number of theoretical models that describe the exact mechanisms by which magnetars can generate impulsive radio emission (see, e.g., Zhang 2020). However, at this point it is unclear if repeating FRBs and apparent non-repeaters share a common origin. Likewise, it is debatable whether the population as a whole is due to a single progenitor type and emission mechanism.

Besides studying the properties of the bursts themselves, the origin(s) of FRBs can be investigated by identifying their host galaxies and local environments. Localizations of apparently one-off FRBs can be achieved by detecting them with wide-field-of-view interferometric arrays operating at high time resolution, such as the Deep Synoptic Array (DSA; e.g. Sharma et al. 2024), the Australian Square Kilometre Array Pathfinder (ASKAP; e.g. Gordon et al. 2024), and the Canadian Hydrogen Intensity Mapping Experiment FRB system (CHIME/FRB) and its Outrigger telescopes (e.g., Shah et al. 2025). To determine the local neighbourhood of an FRB source, within its host, a localization precision on the milliarcsecond (mas) level is needed. This can only be achieved using very long baseline interferometry (VLBI), with baselines of hundreds to thousands of kilometres. The CHIME Outriggers system is now starting to provide ~ 100 mas FRB positions (Andrew & CHIME/FRB Collaboration 2025). The most precise localisations of repeaters, and their sometimes associated compact persistent radio sources (PRS), have been achieved with the European VLBI Network (EVN), as we do in this paper (Marcote et al. 2017, 2020; Kirsten et al. 2022; Nimmo et al. 2022; Bhandari et al. 2023; Hewitt et al. 2024a,b).

With the EVN, it is sometimes possible to localise repeating sources to a few-mas precision, which provides detailed matching to space-based optical and infrared imaging (Tendulkar et al. 2021) and VLBI radio imaging (Bhandari et al. 2023). This gives a zoomed-in view of how the FRB is situated with respect to local star formation and other galactic features like a PRS. In general, the (local) environments of FRBs are diverse, ranging from globular clusters (Kirsten et al. 2022), to massive star-forming galaxies (Sharma et al. 2024), to low-metallicity dwarf galaxies (Tendulkar et al. 2017), and quiescent elliptical galaxies (Shah et al. 2025; Eftekhari et al. 2025). The association of some repeaters with a PRS suggests that the FRB source is also powering a surrounding nebula or jetted outflow due to accretion (see Bhandari et al. 2023, and references therein).

Among repeating FRBs, a rare subset of a few sources show orders-of-magnitude higher burst rate than other repeaters. They are colloquially called ‘hyperactive’ repeaters, with two prominent examples being FRB 20201124A (e.g., Xu et al. 2022) and (e.g., Konijn et al. 2024) FRB 20220912A, both discovered by CHIME/FRB. One of these hyperactive repeating FRB sources is another CHIME/FRB discovery, FRB 20240114A (Shin & CHIME/FRB Collaboration 2024; Shin et al. 2025). Since its discovery, CHIME/FRB has detected a handful of bursts from this

source¹, while thousands more have been detected by various telescopes worldwide (e.g., Ould-Boukattine et al. 2025, Kumar et al. 2024, Xie et al. 2024 and Zhang et al. 2024).

Using MeerKAT, Tian et al. (2024b) were able to robustly localize FRB 20240114A, with an uncertainty of $1.4''$, to a galaxy named J212739.84+041945.8 in the Sloan Digital Sky Survey (SDSS). Bhardwaj et al. (2024a) used the Gran Telescopio CANARIAS (GTC) to determine that the host is a dwarf star-forming galaxy at a redshift of $z = 0.13$. Co-located continuum radio emission was found using the upgraded Giant Metrewave Radio Telescope (uGMRT; Bhusare et al. 2024) and an apparent compact PRS was found at ~ 5 GHz using the Very Long Baseline Array (VLBA; Bruni et al. 2025). Using the GTC, Chen et al. (2025) find a redshift that is consistent with Bhardwaj et al. (2024a) and show that the host of FRB 20240114A is located behind a galaxy cluster.

In this paper, we present a $\sim 90 \times 30$ -mas ($1\text{-}\sigma$) localization of FRB 20240114A using the EVN, which is hundreds of times more precise than the previous localisation of this source. We complement this precise position with new, deep spectroscopic observations of the host galaxy and surrounding field using the GTC. We show that the host is a low-metallicity dwarf galaxy that is a satellite of a more massive central galaxy — analogous to the Large Magellanic Cloud and Milky Way system. The radio and optical observations are described in §2.1 and §2.2, respectively. The data analysis and results are presented in §3 and §3.2. Finally, we discuss the implications of these observations in §4. Throughout this analysis, we adopt Planck 2015 cosmological parameters ($H_0 = 67.8$ km/s/Mpc, $\Omega_m = 0.308$, $\Omega_\Lambda = 0.692$; Planck Collaboration et al. 2016).

2. OBSERVATIONS

2.1. EVN Observations

We observed FRB 20240114A at two epochs in February 2024 using an *ad-hoc* sub-array of EVN dishes (EVN-Lite mode), as part of the PRECISE project (Pinpointing REpeating CHime Sources with EVN dishes; PI: F. Kirsten). Both observing runs were carried out between 1254–1510 MHz in a mixed frequency setup (see Appendix). All stations recorded raw voltages as 2-bit samples, storing both left and right circular polarisations in VDIF format (Whitney et al. 2010).

Epoch 1 (PRECISE code PR318A; EVN code EK056A) was conducted on 15 February 2024 (MJD 60355) with the following stations: Effelsberg (Ef; Germany), Toruń (Tr; Poland), Onsala (O8; Sweden), Westerbork RT-1 (Wb; The Netherlands), Noto (Nt; Italy), Irbene (Ir; Latvia) and six e-MERLIN stations (Cambridge (Cm), Darnhall (Da), Defford (De), Knockin (Kn), Pickmere (Pi), and Jodrell Bank Mark II (Jm); United Kingdom). During Epoch 1, the antenna pointing position towards FRB 20240114A was $\alpha = 21^{\text{h}}27^{\text{m}}39^{\text{s}}.888$, $\delta = +04^{\circ}21'00''.36$ (J2000), which is the CHIME/FRB baseband position of the source (Shin & CHIME/FRB Collaboration 2024).

Epoch 2 (PR319A/EK056B) was conducted on 20 February 2024 (MJD 60360) with the same stations as in Epoch 1, but with the addition of the Tianma 65-metre Telescope (T6; China), which participated for only part of the observation due to elevation limits. The antenna pointing position for Epoch 2 was $\alpha = 21^{\text{h}}27^{\text{m}}39^{\text{s}}.8367$, $\delta = +04^{\circ}19'46''.2333$ (J2000), derived from the MeerKAT burst positions reported in Tian et al. (2024a).

We used phase-referencing with a non-conservative cycle time of ~ 8 minutes, where ~ 6 minute scans on FRB 20240114A are interleaved with ~ 2 minute phase-calibrator scans on J2125+0441 (0.65° away from FRB 20240114A; quoted times are including telescope slewing, see Appendix). The ~ 8 minute cycle time is relatively long and was chosen to maximize the time on FRB 20240114A. Additionally, we observed J2120+0246 roughly twice per hour and used it as a check-source to verify the astrometric solutions. The source J1829+4844 was used as a fringe finder and bandpass calibrator and the flux calibrator 3C286 (J1331+3030) was observed with the e-MERLIN stations. Various pulsars (Appendix) were observed to verify the data quality, frequency setup and burst-search pipeline. We achieved a total on-source time with the Effelsberg telescope (the largest dish in the array) of 200 minutes during Epoch 1 and 202 minutes during Epoch 2.

2.2. GTC Observations

We obtained the spectra of the galaxies considered in this work (§3.3) using the Optical System for Imaging and low-intermediate Resolution Integrated Spectroscopy (OSIRIS+) instrument installed at the GTC (program GTCMULTIPLE2G-24A). The observations were performed on July 4, 2024, under clear conditions with seeing of $\sim 0.7''$. We acquired 4×800 second exposures using the R1000B grism, which covers the spectral range 3630–7000 Å.

¹ <https://www.chime-frb.ca/repeaters/FRB20240114A>

The spectra were obtained with the $1.2''$ slit width, providing a spectral resolution of about 9 \AA . Data reduction was performed with the standard Image Reduction and Analysis Facility (IRAF) routines. The wavelength solution was achieved using a set of HgAr and Ne arc lamps, with a resulting rms of $\lesssim 0.2 \text{ \AA}$. The flux was calibrated using the Feige 110 spectrophotometric standard (Oke 1990).

3. ANALYSIS AND RESULTS

3.1. Radio Analysis and Results

3.1.1. Search for Bursts

The raw voltage data from the Effelsberg telescope were transported to a dedicated server at Onsala Space Observatory (Sweden) to be searched for FRBs. The data were converted to Stokes I (intensity) filterbank files (Lorimer 2011), using `digifil` (van Straten & Bailes 2011). The resulting files had a time and frequency resolution of $64 \mu\text{s}$ and 62.5 kHz , respectively. The intensity data were searched for FRBs with `Heimdall` (Barsdell & Jameson 2024), using a dispersion measure (DM) range of $527.7 \pm 50 \text{ pc cm}^{-3}$. FRB-candidates identified as such by `Heimdall` were further analysed by `FETCH` (Agarwal et al. 2020), a deep-learning-based transient classifier. We manually inspect all candidates for which `FETCH` assigned a ≥ 0.5 probability that the candidate was of astrophysical origin. The full details of the pipeline are described in Kirsten et al. (2021, 2022). We detected 6 bursts in Epoch 1 and 13 bursts in Epoch 2. These bursts are labelled A01–A07 and B01–B13 for the first and second epoch, respectively. Burst A02 was initially picked up by the pipeline but during the analysis the burst was deemed too weak to be confidently labelled as a real FRB and was therefore removed from the sample.

3.1.2. Interferometric Data

After the bursts were detected, the baseband data of all participating stations were transferred to the Joint Institute for VLBI ERIC (JIVE; The Netherlands) for correlation with the FX Software Correlator `SFXC` (Keimpema et al. 2015). The calibrator data were correlated using 2-s integrations and 0.5-MHz channel widths (64 channels per 32 MHz subband). Using the delay-mapping technique described in Marcote et al. (2017, 2020), we derived a rough (arcsecond-level precision) position, $\alpha = 21^{\text{h}}27^{\text{m}}39^{\text{s}}.9$, $\delta = +04^{\circ}19'43''.4$ (J2000), for the brightest burst of Epoch 1 (A04). The data of the brightest burst were re-correlated at that position. Those data were reduced, calibrated and imaged with `CASA` (McMullin et al. 2007) — following the same calibration strategy as described in Bhandari et al. (2023) — leading to a best position of that single burst of $\alpha = 21^{\text{h}}27^{\text{m}}39^{\text{s}}.835$, $\delta = +04^{\circ}19'45''.634$ (J2000, with a $1\text{-}\sigma$ uncertainty of $\sim 200 \text{ mas}$; Snelders et al. 2024). The final correlation, of both the continuum data and the burst data of FRB 20240114A, were referenced to a phase-center of $\alpha = 21^{\text{h}}27^{\text{m}}39^{\text{s}}.835$, $\delta = +04^{\circ}19'45''.634$ (J2000), using the same frequency resolution as the calibrator data. The continuum data have 2-s integrations; the burst data were coherently dedispersed, using a DM of 527.7 pc cm^{-3} , and correlated using various ‘gates’ that depend on the temporal widths and arrival-times of the bursts.

The correlated data were processed and calibrated with `AIPS` (Greisen 2003). We made use of the standard EVN calibration table, which contains parallactic angle corrections and *a-priori* gain correction, using the gain curves and system temperature measurements that the stations recorded during the observations. We also make use of the EVN flagging table, flagging all data from antennas which were still slewing. Additionally, we flagged 18.5% (6 channels on each side) at the edges of the subbands, where antenna sensitivity significantly drops. Similarly to most FRB VLBI papers (e.g., Hewitt et al. 2024b), we made use of the `AIPS` task `VLBATECR` to correct for ionospheric dispersive delays, taking into account recent developments from Petrov (2023).

The interferometric data of the ‘fringe-finder’ (J1829+4844) and ‘phase-calibrator’ (J2125+0441) were inspected and flagged for radio frequency interference (RFI) using the `AIPS` tool `spflag`, which allows the user to flag visibilities as a function of time, frequency and baseline. In the first step of the calibration the instrumental delay between subbands is removed using the fringe-finder scan. Next, the phase-calibrator scans are used to derive phase-solutions as a function of time and frequency for the entire observation. The phase-calibrator was imaged using `DIFMAP` (Shepherd 1997) to construct a model of the phase-calibrator that was used for self-calibration.

The calibration solutions were transferred to the interferometric data of the bursts. We exported the flagged and calibrated burst visibilities as `UVFITS` files with `fittp` and imported them in `CASA` with `importuvfits`. We chose this approach because the Pythonic interface of `tclean` (the imaging tool of `CASA`) facilitates the iteration over burst visibilities as a function of ‘scan’ (in this case individual bursts) and/or antenna configuration.

We image each burst individually using `tclean` with a natural weighting scheme, creating so-called ‘dirty’ maps. We opt to only image using just three baselines; Effelsberg to Noto, Toruń and Onsala. We do this for a multitude of reasons; These are the only antennas that recorded all the bursts, recorded the widest bandwidth and since Effelsberg is so much more sensitive than the smaller antennas, including the baselines between Noto, Toruń and Onsala does not change the dirty maps in any meaningful way. For each burst, we image 4096×4096 pixels using a cell size of 1 mas and use the position quoted in [Snelders et al. \(2024\)](#) as the phase-center. In Figure 1 we show the absolute value of the dirty maps of each burst. Burst B08 is not shown since no calibration solution was found in one of the neighbouring phase-calibrator scans.

We attempted to combine the calibrated burst visibilities before imaging — similar to, e.g., [Nimmo et al. \(2022\)](#) and [Kirsten et al. \(2022\)](#). However, this actually decreased the quality of the images. This also happened when only bursts with a clear cross fringe pattern (e.g., B07 and B09) were combined. We attribute this to imperfect calibration of ionospheric phase variations. A significant contributing factor to this was the distance between the Sun and the target: $\sim 18^\circ$ during the observations, much less than the recommended $\sim 50^\circ$ for VLBI observations at these radio frequencies (~ 1.4 GHz). Additionally, the target elevation was rather low (below 25°) at the start of both observations (Figure 6). Finally, the observations took place close to the expected maximum of Solar Cycle 25², and during the observations the solar wind conditions were changing rapidly³.

To combine multiple bursts ‘incoherently’, we first manually identify bursts that individually have a clear cross fringe pattern: A04 for Epoch 1 and B04, B06, B07, B09 and B13 for Epoch 2. For each of these bursts we fit a rotated two dimensional Gaussian function to all pixels where the absolute value of the dirty map of the burst is above $3\text{-}\sigma$ (as in [Nimmo et al. 2022](#); [Hewitt et al. 2024b](#)). The $2\text{-}\sigma$ uncertainty regions of those fits are shown as gold ellipses in Figure 1. To combine the Gaussians we multiply the individual probabilities per pixel and fit the resulting probability with a rotated two-dimensional Gaussian.

Our best position for FRB 20240114A is: $\alpha = 21^{\text{h}}27^{\text{m}}39^{\text{s}}.835$, $\delta = +04^\circ19'45''.668$ (J2000, ICRF).

The $1\text{-}\sigma$ uncertainty of that position is described by a two dimensional Gaussian with a major axis of 93 mas and minor axis of 28 mas that has been rotated by 27° (Figure 1). The $2\text{-}\sigma$ uncertainty region of the best position is shown as a white ellipse in Figure 1. For almost all bursts the ellipse is on top of a fringe (e.g., A03) further illustrating the robustness of our localization. The angular separation between the VLBA C-band PRS detection ([Bruni et al. 2025](#)) and our best position is 13 mas, well within our $1\text{-}\sigma$ uncertainty region.

We do not search for a PRS in the continuum data since the interferometric burst data showed that calibration solutions were imperfect throughout the observations — likely due to a rapidly changing ionosphere. Even with a hypothetical perfect calibration the expected thermal noise in the continuum data would be $\sim 20 \mu\text{Jy/beam}$ (400 minute integration time with the Effelsberg, Noto, Toruń and Onsala telescopes) — which is not sensitive enough to statistically claim the existence of a PRS based on the flux densities quoted in [Bruni et al. \(2025\)](#), [Bhusare et al. \(2024\)](#) and [Zhang & Yu \(2024\)](#).

3.1.3. Burst Properties

We use `DM_phase` ([Seymour et al. 2019](#)) to determine the DM of burst B07 (the brightest burst in our sample) and find a DM of $527.723 \pm 0.042 \text{ pc cm}^{-3}$. We then use `SFXC` to coherently dedisperse the baseband data of just the Effelsberg telescope to create Stokes I (total intensity) files for every burst. These files have a time and frequency resolution of $32 \mu\text{s}$ and 500 kHz, respectively, and are written out as `sigproc` filterbank files with 32-bit floating-point numbers. The dynamic spectra of the bursts are shown in Figure 2 where they are further averaged in time to increase their visibility. For every burst we determine their time-of-arrival, width, signal-to-noise ratio (S/N), fluence, spectral luminosity and peak flux density and tabulate the results in Table 1.

3.2. FRB DM Budget

As noted in § 3.1.3, FRB 20240114A has an observed dispersion measure, DM_{obs} , of $527.723 \pm 0.042 \text{ pc cm}^{-3}$. This value is unexpectedly large given the modest Galactic foreground and the low redshift of the host galaxy, as highlighted

² <https://www.swpc.noaa.gov/news/solar-cycle-25-forecast-update>

³ <https://www.swpc.noaa.gov/products/real-time-solar-wind>

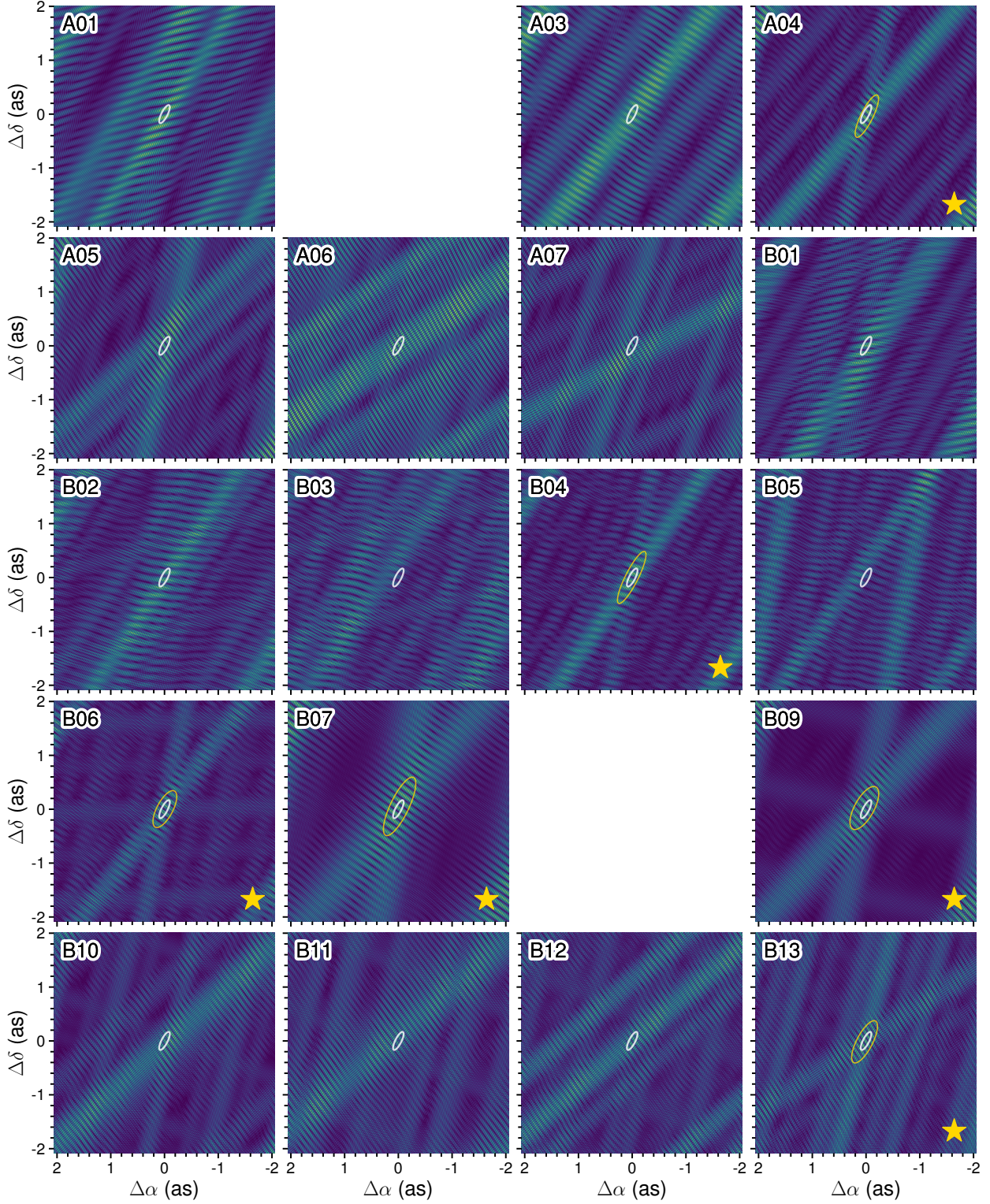


Figure 1. Each panel shows the absolute value of the dirty maps (i.e., the absolute value of the Fourier transform of the visibilities) for individual bursts. Bursts from Epoch 1 (EK056A/PR318A) are labelled A_n and bursts from Epoch 2 (EK056B/PR319A) are labelled B_n . The bursts are sorted on their arrival times. Bursts that pass the visual inspection (as indicated by gold stars) are fitted with a rotated 2-D Gaussian function, for which the 2- σ contour are shown as gold ellipses. The 2- σ region of the best combined position is shown as a white ellipse in all panels. Burst A02 was not found to be robustly astrophysical in origin (§3.1.1) and no calibration solution was found for B08 (§3.1.2). Consequently, these panels are left blank.

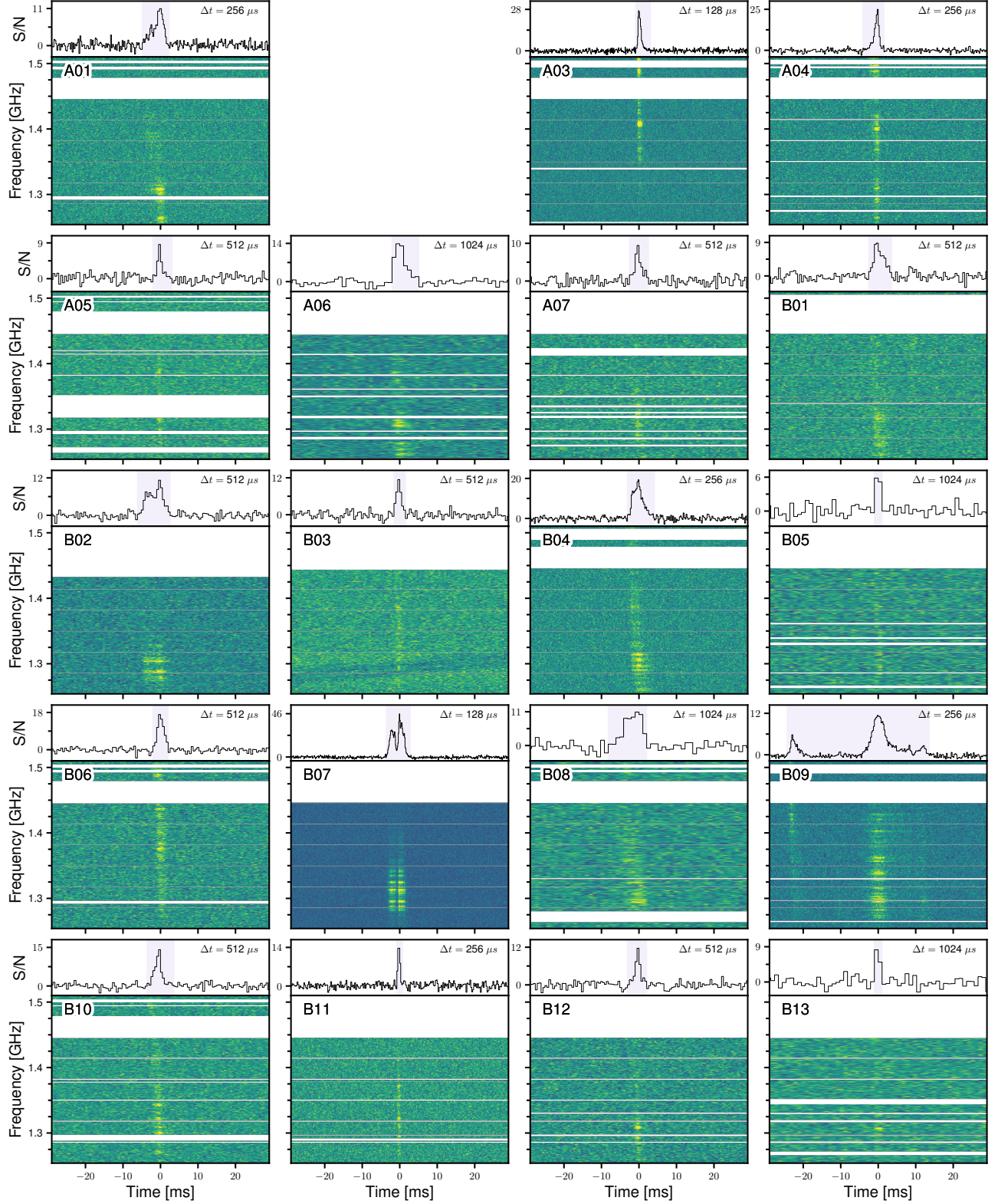


Figure 2. Dynamic spectra (bottom panels) and frequency-averaged temporal profiles (top panels) for all bursts. Each burst is coherently dedispersed to a value of $527.723 \text{ pc cm}^{-3}$. The frequency resolution in each dynamic spectrum is 500 kHz and the respective time resolutions are indicated in the top right of each panel. Horizontal white bands in the dynamic spectra indicate data that have been masked due to RFI or subband edges. Burst labels are the same as in Figure 1. Burst A02 was not found to be robustly astrophysical in origin (§3.1.1). Consequently, this panel is left blank.

Table 1. Burst properties.

Burst label	ToA ^a [MJD]	Det. S/N ^b	Peak S/N ^c	Width ^d [ms]	Fluence ^e [Jy ms]	Peak Flux Density ^e [Jy]	Spectral Luminosity ^{e,f} [10 ³¹ erg s ⁻¹ Hz ⁻¹]
A01	60355.2973790745	29.7	10.9	7.168	1.34	0.44	6.60
A02 ^g		7.3					
A03	60355.3652337659	30.2	27.1	3.968	1.52	1.54	13.60
A04	60355.3940163658	32.2	24.9	5.632	1.44	1.01	9.05
A05	60355.4368167038	11.0	8.6	5.120	0.37	0.27	2.59
A06	60355.4665637667	16.8	13.9	7.168	1.11	0.31	5.50
A07	60355.4823046109	9.5	9.4	5.120	0.60	0.31	4.12
B01	60360.2914847421	17.4	8.8	6.144	0.79	0.26	4.54
B02	60360.3168374267	20.1	11.3	8.704	1.35	0.34	5.50
B03	60360.3262287994	9.5	11.4	3.072	0.52	0.34	5.97
B04	60360.3290625037	44.6	19.3	7.168	2.31	0.78	11.39
B05	60360.3332507559	10.4	5.8	2.048	0.24	0.13	4.23
B06	60360.3567331963	26.2	17.0	4.096	1.01	0.48	8.74
B07	60360.3701272696	7.6	45.8	6.400	6.67	2.71	36.87
B08	60360.3754591768	23.0	10.9	10.240	1.23	0.23	4.24
B09	60360.3965590087	90.9	11.4	37.888	2.66	0.46	2.49
B10	60360.4223725478	15.2	14.1	7.168	0.84	0.41	4.13
B11	60360.4279151582	19.9	13.7	1.536	0.47	0.59	10.88
B12	60360.4282615629	13.7	11.7	5.120	0.56	0.35	3.85
B13	60360.4549215993	18.5	8.2	2.048	0.30	0.18	5.23

^a Corrected to the Solar System Barycenter to infinite frequency assuming a dispersion measure of 527.723 pc cm⁻³, a reference frequency of 1494 MHz, a dispersion measure constant of 1/(2.41 × 10⁻⁴) MHz² pc⁻¹ cm³ s and a source of position of $\alpha = 21^{\text{h}}27^{\text{m}}39^{\text{s}}.835$, $\delta = +04^{\circ}19'45''.634$ (J2000, ICRF).

The times quoted are dynamical times (TDB).

^b The detection signal-to-noise (S/N), as reported by `Heimdall`.

^c The peak value of the time-series, as shown in Figure 2.

^d Manually determined time-span of the burst, shown as the highlighted region in the time-series in Figure 2.

^e We estimate a (conservative) error of 20% for these values, which is dominated by the uncertainty in the system equivalent flux density (SEFD) of the Effelsberg telescope.

^f Using Equation 5 from [Ould-Boukattine et al. \(2024\)](#) and assuming a luminosity distance of 614.6 Mpc ($z = 0.1300$).

^g Burst A02 was removed from the sample (§3.1.1).

by [Tian et al. \(2024b\)](#) and [Chen et al. \(2025\)](#). To explain this excess, we decompose the total DM into five astrophysical components, all evaluated in the observer frame:

$$\text{DM}_{\text{obs}} = \text{DM}_{\text{disk}} + \text{DM}_{\text{halo}} + \text{DM}_{\text{IGM}} + \text{DM}_{\text{fhalo}} + \text{DM}_{\text{host}}. \quad (1)$$

Here, DM_{disk} and DM_{halo} represent the Milky Way disk and halo contributions, respectively. DM_{IGM} arises from the intergalactic medium, DM_{fhalo} reflects excess dispersion from intervening galaxy, group, or cluster halos along the line of sight, and DM_{host} comprises the host galaxy's interstellar medium and circumgalactic halo. Below, we quantify the DM contribution of each component, specify the adopted priors, and propagate their uncertainties to identify the dominant contributor to the total dispersion.

3.2.1. Milky Way Disk and Halo Contributions

For DM_{disk} , we employ a Gaussian prior $\mathcal{N}(\mu_{\text{disk}}, \sigma_{\text{disk}}^2)$, where $\mu_{\text{disk}} = 45 \text{ pc cm}^{-3}$ is the mean of the values predicted by the NE2001 (50 pc cm⁻³; [Cordes & Lazio 2002](#)) and YMW16 (40 pc cm⁻³; [Yao et al. 2017](#)) Galactic free-electron-density models. We adopt a conservative fractional uncertainty of 20 %, yielding $\sigma_{\text{disk}} = 9 \text{ pc cm}^{-3}$. For the Galactic

halo contribution, we follow the analytic prescription of [Yamasaki & Totani \(2020\)](#). In line with previous work (e.g., [Anna-Thomas et al. 2025](#)), we use a uniform prior $\text{DM}_{\text{halo}} \sim \mathcal{U}[22.5, 67.5] \text{ pc cm}^{-3}$, which corresponds to a $\pm 50\%$ systematic uncertainty around the model prediction of $\text{DM}_{\text{halo}} = 45 \text{ pc cm}^{-3}$ along the FRB line of sight.

3.2.2. Intergalactic Medium Contribution

We estimate the DM from the diffuse IGM using the empirical redshift-DM relation ([Macquart et al. 2020](#)). For the host-galaxy redshift at $z = 0.1300$ (§3.3), this formalism yields $\text{DM}_{\text{IGM}} = 95_{-20}^{+55} \text{ pc cm}^{-3}$ (68 % credible region) with a mean $\text{DM}_{\text{IGM}} = 116 \text{ pc cm}^{-3}$ and a standard deviation of $\text{DM}_{\text{IGM}} = 61 \text{ pc cm}^{-3}$. To construct the associated probability-density function, we follow the analytic prescription of [Macquart et al. \(2020\)](#), adopting $\alpha = 3.0$ and $\beta = 3.0$ for the power-law indices of the inner-halo baryon profile, and a baryonic-feedback parameter $F = 0.2$. These parameter choices are consistent with recent FRB studies ([Baptista et al. 2024](#)).

3.2.3. Intervening Halo Contributions

Here we estimate the DM contribution from intervening structures, such as foreground galaxies, groups, or clusters, along the FRB line of sight. [O’Connor et al. \(2024\)](#) utilized CHIME/FRB baseband localization ([Shin & CHIME/FRB Collaboration 2024](#)) and the DESI Legacy Imaging Survey-based cluster catalog of [Wen & Han \(2024\)](#) to identify a candidate foreground galaxy cluster, J212719.9+042225. Subsequent analysis by [Chen et al. \(2025\)](#) confirmed that this cluster likely contributes significantly to the FRB’s DM budget. The cluster, located at a spectroscopic redshift $z = 0.0903$ ([Wen & Han 2024](#)), lies $5.6'$ from the FRB EVN position, well within its virial radius. Therefore, we expect a non-negligible DM contribution from its intracluster medium (ICM).

This cluster has a derived total mass of $M_{500} = 6.8 \times 10^{13} M_{\odot}$ and a radius of $r_{500} = 0.67 \text{ Mpc}$, based on DESI Legacy Imaging Survey data ([Wen & Han 2024](#)). Here, M_{500} represents the total mass enclosed within a sphere of radius r_{500} , where the average matter density is 500 times the critical density of the Universe at the cluster’s redshift.

To quantify the DM contribution from the ICM of J212719.9+042225, we model the electron density distribution using a spherical β -model:

$$n_e(r) = n_{e0} \left[1 + \left(\frac{r}{r_c} \right)^2 \right]^{-3\beta/2}, \quad (2)$$

where n_{e0} is the central electron density, r_c is the core radius, and β is the slope parameter. We adopt $\beta = 0.67$, consistent with [Cavaliere & Fusco-Femiano \(1976\)](#) and [Sarazin \(1986\)](#). The core radius is assumed to be $r_c = 0.1 r_{500}$, following common practice in X-ray studies of galaxy clusters (e.g., [Mohr et al. 1999](#); [Vikhlinin et al. 2006](#)). The normalization n_{e0} is derived by imposing that the integrated gas mass within r_{500} equals a fraction f_{gas} of the total cluster mass:

$$f_{\text{gas}} M_{500} = 4\pi \mu_e m_p \int_0^{r_{500}} n_e(r) r^2 dr, \quad (3)$$

where we adopt $f_{\text{gas}} = 0.12$ ([Allen et al. 2004](#); [Vikhlinin et al. 2006](#)), $\mu_e \approx 1.167$ is the reduced mass after accounting for fully ionized helium and hydrogen, and m_p is the proton mass.

Using this electron density model and converting the FRB’s angular offset into a projected distance of 588 kpc, our numerical integration yields an estimated ICM DM of $\text{DM}_{\text{ICM}} \approx 66 \text{ pc cm}^{-3}$. Alternatively, in the observer frame, $\text{DM}_{\text{ICM}} \approx 60 \text{ pc cm}^{-3}$.

Next, we searched for additional foreground groups. No such groups were found in the SDSS DR12 and 2MRS catalogs ([Saulder et al. 2016](#)) that had a reported group radius exceeding its angular offset from the FRB. We then queried the DESI Legacy Imaging Survey photometric redshift catalog ([Zou et al. 2019](#)) for galaxies within 2° of the FRB position. We selected galaxies satisfying $z_{\text{photo}} - 2\sigma_z < 0.13$, where 0.13 is the host redshift (§3.3). For each candidate, we computed the ratio of its effective (half-light) radius to the projected angular offset from the FRB, hereafter referred to as the ‘offset ratio’. We selected galaxies with offset ratios exceeding the empirically measured stellar-to-halo radius ratio (SRHR) of 0.018 at $z \sim 0.1$ ([Somerville et al. 2018](#)), yielding eight candidates whose virial radii overlap with the FRB sight line (Appendix A). Their individual DM contributions are estimated in Appendix A, yielding a total DM contribution from the foreground galaxy halos of $\text{DM}_{\text{c,halo}} = 135 \pm 68 \text{ pc cm}^{-3}$.

Hence, the total intervening-halo contribution is:

$$\text{DM}_{\text{fhalo}} = \text{DM}_{\text{c,halo}} + \text{DM}_{\text{ICM}} = 60 + (135 \pm 68) \text{ pc cm}^{-3}.$$

Among the eight foreground galaxies, one galaxy, DESI J212740.488+041911.64 (hereafter ‘the central galaxy’), is located just $35.5''$ from the FRB host and is classified as a spiral based on its morphology in DESI images (Cai et al. 2025). Given its sky proximity to the FRB host and their small photometric redshift difference, the central galaxy may share the same dark-matter halo as the FRB host. We analyze the spectroscopic properties of this central galaxy and its relationship to the FRB host in detail in §3.3 and further discuss their potential shared halo in §3.5.

3.2.4. Host Galaxy Contribution

We estimate the contribution of the FRB 20240114A host galaxy to the observed DM using both emission-based diagnostics and a DM budget subtraction.

We begin by modeling the host galaxy’s surface brightness profile. A Sérsic profile fit with index $n = 1$ to the DESI Legacy Survey r -band image yields an effective angular radius of $a = 0.4''$. Within a circular aperture of this radius, we measure an extinction-corrected $H\alpha$ flux of $F = (1.54^{+0.10}_{-0.08}) \times 10^{-16} \text{ erg s}^{-1} \text{ cm}^{-2}$. Dividing by the aperture area, $\pi a^2 \simeq 0.503 \text{ arcsec}^2$, gives an observed surface brightness of $S'_{\text{obs}} \simeq 54.1^{+3.5}_{-2.8} \text{ Rayleigh}$. After correcting for cosmological surface-brightness dimming via $(1+z)^4$ with $z = 0.1300$ (§3.3), we obtain a source-frame surface brightness of $S(H\alpha)_{\text{source}} \simeq 88.1^{+5.7}_{-4.6} \text{ Rayleigh}$.

This value is converted to an emission measure (EM) using the relation appropriate for a warm ionized medium at $T = 10^4 \text{ K}$ (Reynolds 1977):

$$\text{EM} = 2.75 \text{ pc cm}^{-6} \left(\frac{T}{10^4 \text{ K}} \right)^{0.9} \left[\frac{S(H\alpha)_{\text{source}}}{\text{Rayleigh}} \right],$$

yielding $\text{EM} \simeq 242^{+16}_{-13} \text{ pc cm}^{-6}$.

To translate EM into a DM, we adopt the model:

$$\text{DM}_{\text{host}} = \sqrt{\frac{\text{EM} L}{A}},$$

where $L = 2a = 1.84 \times 10^3 \text{ pc}$ is the physical path length through the emitting region, and $A = \zeta(1 + \epsilon^2)/f$ encodes the microphysical properties of the ionized gas. Following Cordes et al. (2022), we impose a flat prior $A \in [1, 50]$ and marginalize to obtain $\text{DM}_{\text{host}} = 132^{+92}_{-29} \text{ pc cm}^{-3}$.

In the observer frame, this corresponds to a host contribution of:

$$\text{DM}_{\text{host, obs}} = \frac{\text{DM}_{\text{host}}}{1+z} = 117^{+81}_{-26} \text{ pc cm}^{-3}.$$

Adding the contribution from the host’s circumgalactic halo, estimated to be 9 pc cm^{-3} in the observer frame (Appendix A), we find a total host-frame contribution of $\text{DM}_{\text{host, obs}} = 126^{+81}_{-26} \text{ pc cm}^{-3}$.

We independently verify this estimate using a DM budget analysis:

$$\text{DM}_{\text{host, obs}} = \text{DM}_{\text{obs}} - (\text{DM}_{\text{disk}} + \text{DM}_{\text{halo}} + \text{DM}_{\text{IGM}} + \text{DM}_{\text{fhalo}}).$$

Adopting mean values for these components from §3.2.1, §3.2.2, and §3.2.3 as $\{45, 45, 116, 195\} \text{ pc cm}^{-3}$ respectively, the sum of these foreground DM terms is $\sum_i \text{DM}_i = 401 \text{ pc cm}^{-3}$. The combined uncertainty is $\sigma_{\text{fore}} = \sqrt{9^2 + 22.5^2 + 61^2 + 68^2} \approx 95 \text{ pc cm}^{-3}$.

Subtracting from $\text{DM}_{\text{obs}} = 527.72 \pm 0.04 \text{ pc cm}^{-3}$, we obtain $\text{DM}_{\text{host, obs}} \approx 126 \pm 95 \text{ pc cm}^{-3}$. This subtraction-based value is in good agreement with the $H\alpha$ -derived estimate, lending confidence to both methods. The substantial host contribution inferred from these independent approaches suggests a dense, ionized environment local to the FRB source, which, when combined with other FRB observables, can provide meaningful constraints on the ionization state and baryonic content of its host galaxy.

This comprehensive FRB DM budget analysis provides a robust framework for understanding the total observed dispersion of FRB 20240114A, highlighting the significant contributions from both intervening structures and the host galaxy itself.

3.3. GTC Spectroscopic Analysis of the FRB Host and Central Galaxy

We used the reduced 2-D, long-slit spectrum to extract two apertures, corresponding to the spectra of the central galaxy and the FRB host. These apertures were $2.0''$ and $2.9''$ along the slit, respectively, with a width of $1.23''$, and were centered on the positions of maximum emission for each target.

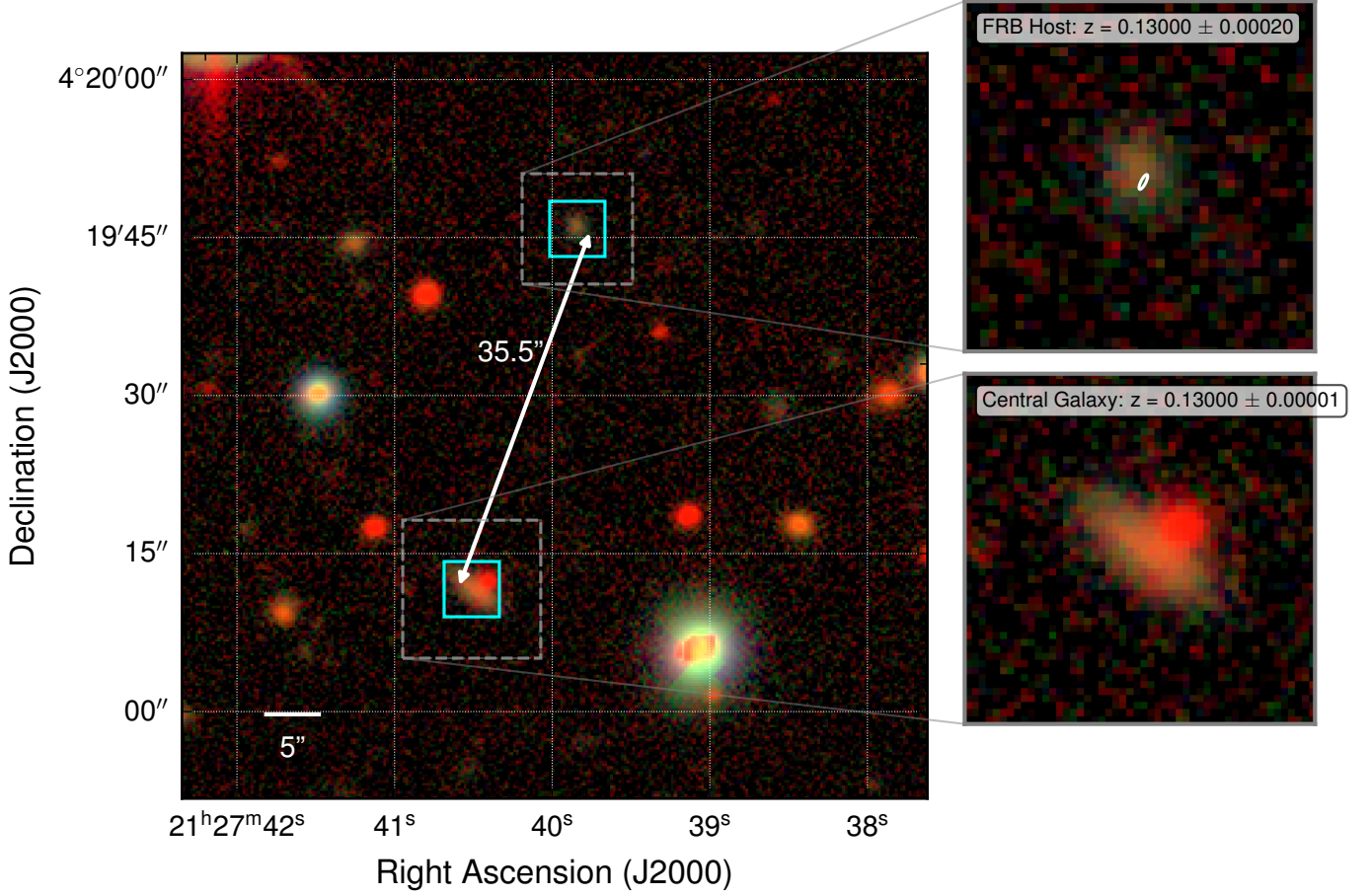


Figure 3. Wide-field RGB view of the FRB 20240114A field using DESI g (blue), r (green), and z (red) band images. The FRB host galaxy at $z = 0.1300$, likely a satellite of a nearby central galaxy at the same systemic redshift, is marked with a cyan box along with its companion; their projected separation of $35.5''$ (85 kpc transverse distance) is marked by the double-headed arrow. Gray dashed boxes indicate the zoom regions shown in the upper (host) and lower (central galaxy) insets. In the host inset, the EVN-derived FRB position is highlighted by a white ellipse whose semi-axes represent the $10\text{-}\sigma$ localization uncertainty (inflated to be visible on this scale).

Given the relatively low continuum signal in both spectra, we could not model the continuum emission using stellar population synthesis. Instead, we obtained the parameters of the detected emission lines by analyzing the emission above a low-order polynomial continuum. Line fluxes were measured by adding all flux above the best-fitting continuum within specific spectral windows (direct flux measurements). Alternatively, we also measured line fluxes by fitting an analytical function to the profile using the LMFIT Python package (Newville et al. 2021). For these fits, we used both single Gaussians and more complex Gauss-Hermite profiles, which account for non-zero skewness and kurtosis. Unless otherwise stated, we use either direct measurements or single-Gaussian fits, depending on the signal-to-noise ratio (S/N) or equivalent width of the line. For determining radial velocities, however, we exclusively rely on single-Gaussian (1G) fits, as they are more robust against noise than Gauss-Hermite profile fits.

Figure 4 shows the spectra of the two regions with detected lines along the slit, using the extraction parameters listed above. We also present the results of the 1G fits for most of the emission lines detected in these spectra. The measured radial velocities and line fluxes are provided in Table 2.

Based on the detected emission lines, we measure a redshift of $z = 0.13000 \pm 0.00020$ for the FRB host and $z = 0.1297 \pm 0.0003$ for the central galaxy. The central-galaxy value is in excellent agreement with the DESI DR1 FastSpecFit catalog (Moustakas et al. 2023), which reports $z = 0.13000 \pm 0.00001$. However, previous studies estimated slightly higher values for the FRB host: Chen et al. (2025) find $z = 0.1306 \pm 0.0002$ and Bruni et al. (2025) report $z = 0.13056 \pm 0.00003$. These correspond to velocity offsets of $\sim 180 \text{ km s}^{-1}$, which far exceed our arc-lamp calibration rms of $\lesssim 0.1 \text{ \AA}$ ($\sim 5 \text{ km s}^{-1}$). Such shifts can be explained by sub-arcsecond slit-filling and centering errors combined

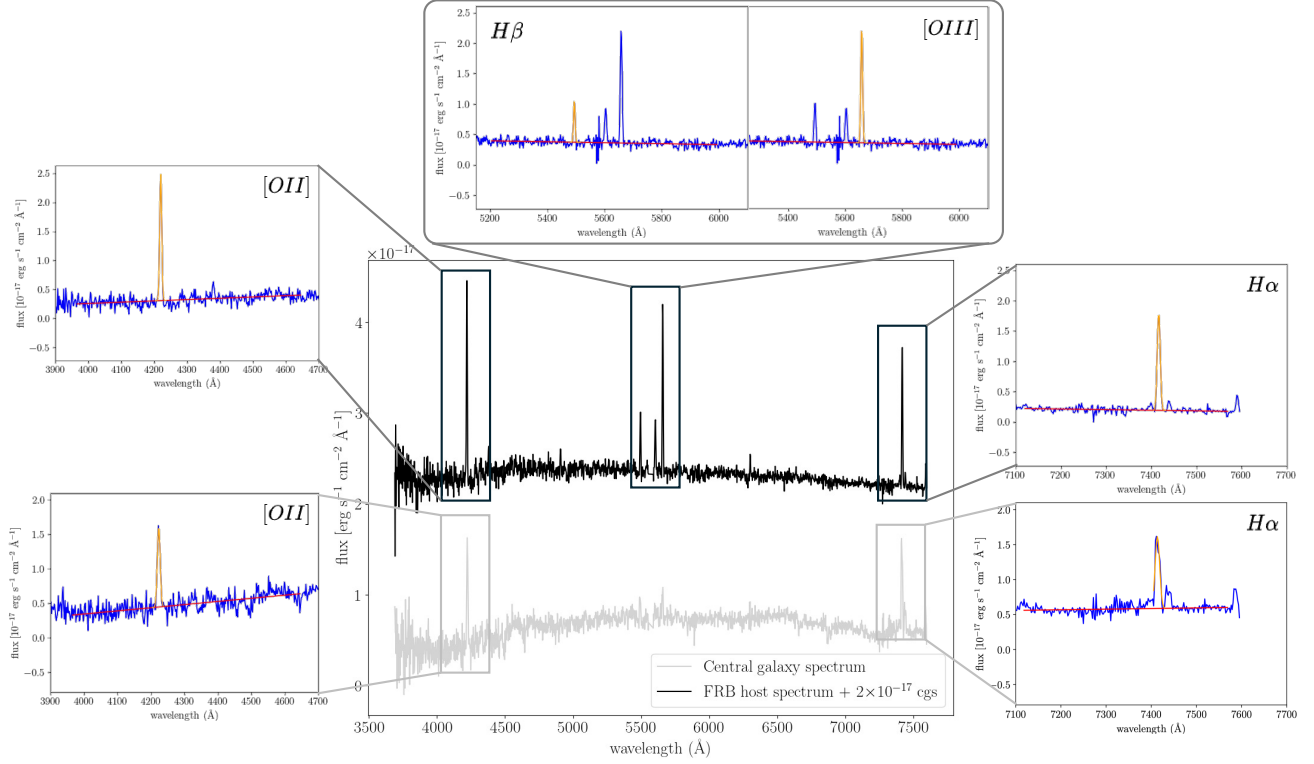


Figure 4. Central panel: OSIRIS spectra of the FRB host (black solid line) and the central galaxy (solid grey). Peripheral panels: These insets show the brightest emission lines detected in each spectrum and their corresponding single-Gaussian fits. On the left, we show the region around the unresolved $[\text{OII}]\lambda\lambda 3726,3629\text{\AA}$ doublet, while the $\text{H}\beta$ and $[\text{OIII}]\lambda\lambda 4959,5007\text{\AA}$ lines and their best fits are shown on top. The right panels show the $\text{H}\alpha$ line region for each of the two spectra.

Table 2. Line radial velocities and fluxes of the FRB host and the central galaxy.

Line	v_{helio} [km s ⁻¹]	δv	f_{data} [10 ⁻¹⁷ erg s ⁻¹ cm ⁻²]	δf_{data}	EW [Å]	δEW	$f_{1\text{G}}$ [10 ⁻¹⁷ erg s ⁻¹ cm ⁻²]	$\delta f_{1\text{G}}$	EW _{1G,c} [Å]	$f_{\text{data,c}}$ [10 ⁻¹⁷ erg s ⁻¹ cm ⁻²]	$f_{1\text{G,c}}$
FRB host											
[OII]	39670	7	15.8	1.300	51.2	5.4	17.0	1.320	55.0	20.1	21.6
Hβ	39048	12	4.00	0.614	13.8	1.7	4.72	0.621	15.7	6.08	6.93
[OIII]	39013	4	14.6	0.753	40.5	2.4	15.1	0.758	41.9	17.2	17.8
Hα	39016	4	13.2	0.648	70.6	5.1	13.5	0.652	72.1	15.3	15.6
[NII]	38992	12	1.05	0.356	5.5	1.9	1.09	0.357	5.8	1.18	1.23
[SII]	39017	11	1.45	0.421	8.3	2.5	1.65	0.425	9.4	1.62	1.85
Central galaxy											
[OII]	39941	15	12.2	1.460	27.4	3.6	12.5	1.460	28.1	45.3	16.1
Hβ	38858	48	1.07	0.730	4.4	1.0	2.26	0.738	6.0	8.87	5.41
[OIII]	38932	39	3.57	0.789	4.9	1.1	3.22	0.787	4.4	9.23	3.85
Hα	38887	23	12.1	0.745	22.6	1.4	12.5	0.748	23.2	26.5	15.5
[NII]	38906	37	3.54	0.724	6.0	1.2	3.58	0.724	6.1	7.03	4.06
[SII]	38839	18	2.41	0.553	4.0	0.9	2.44	0.554	4.1	4.70	2.76

with finite spectral resolution — e.g., a $0.2''$ misalignment at $R \approx 235$ yields $\sim 180 \text{ km s}^{-1}$, while $R \sim 1000$ requires $\sim 0.7''$ — and by uncorrected atmospheric refraction. Although our R1000B setup ($R \approx 550$, $1.2''$ slit centered on the continuum peak) is less susceptible, residual systematics of tens of km s^{-1} remain. In light of these considerations

Table 3. Major observables of the FRB 20240114A host and its central galaxy.

Parameter	FRB Host	Central Galaxy
R.A. (J2000)	21 ^h 27 ^m 39 ^s .84	21 ^h 27 ^m 40 ^s .49
Dec. (J2000)	+04°19′45″.8	+04°19′11″.6
Galaxy name	DESI J212739.84+041945.8	DESI J212740.49+041911.6
Apparent r -band mag (m_r , AB) ^a	21.94	20.03
Galactic r -band extinction (A_r , AB) ^a	0.16	0.16
Spectroscopic redshift (z_{spec})	0.1300 ± 0.0002	0.13000 ± 0.00001 ^d
Absolute r -band mag (M_r , AB)	−17.06	−18.97
Effective radius, R_{eff} (kpc) ^a	0.9	4.3
SFR ($\text{H}\alpha$; $M_{\odot} \text{ yr}^{-1}$) ^b	0.061 ^{+0.004} _{−0.003}	0.16 ^{+0.07} _{−0.01}
SFR (0–100 Myr; $M_{\odot} \text{ yr}^{-1}$) ^c	0.06 ^{+0.06} _{−0.04}	0.52 ^{+0.70} _{−0.27}
Stellar mass $\log(M/M_{\odot})$ ^c	8.55 ^{+0.12} _{−0.14}	9.83 ^{+0.09} _{−0.10} ^c
Stellar metallicity $\log(Z/Z_{\odot})$ ^c	−1.24 ^{+0.36} _{−0.52}	−1.01 ^{+0.33} _{−0.35} ^c
Gas-phase metallicity $\log(Z/Z_{\odot})_{\text{gas}}$ ^b	−0.47 ± 0.13	−0.23 ± 0.13
Mass-weighted age (Gyr) ^c	5.79 ^{+0.94} _{−1.24}	6.03 ^{+0.85} _{−1.65}
$\log(\text{sSFR}_{0-100 \text{ Myr}}) (\text{yr}^{-1})$ ^c	−9.76 ^{+0.44} _{−0.49}	−10.11 ^{+0.47} _{−0.41}
A_V (young stars; mag) ^c	0.11 ^{+0.14} _{−0.08}	1.12 ^{+0.32} _{−0.32}
Host AGN	N	N

Notes.^a Using data from the DESI Legacy Survey photometric catalog (Zou et al. 2019).^b Obtained from optical spectra (Appendix B).^c Estimated using **Prospector**.^d From the DESI Data Release 1 (DR1) FastSpecFit Spectral Synthesis and Emission-Line Catalog (Moustakas et al. 2023)

— and because our configuration symmetrically samples both sides of the disk and achieves a well-characterized wavelength solution — we adopt $z = 0.13000 \pm 0.00020$ as the systemic redshift of the FRB host in all our analyses.

The line fluxes have been first corrected for foreground Milky Way attenuation, assuming a Galactic color-excess of $E(B - V) = 0.06$ mag and the Cardelli et al. (1989) dust-attenuation law. We then corrected the Balmer-line fluxes for underlying stellar absorption, assuming equivalent widths in absorption for $\text{H}\beta$ and $\text{H}\alpha$ of 3 Å and 2 Å, respectively. Finally, the different fluxes were corrected for internal extinction using the Balmer decrement after adopting an intrinsic $f_{\text{H}\alpha}/f_{\text{H}\beta} = 2.86$. In the case of the FRB host, which is less luminous and likely less metal-rich than the central galaxy, this line ratio is close to the theoretical value for no extinction in some cases. The dust attenuation derived from the Balmer decrement for both galaxies agrees well with the values inferred from our stellar population synthesis. These spectroscopic results, along with our photometric data, form the foundation for characterizing the intrinsic physical properties of the FRB host and the central galaxy, which we discuss in detail in §3.4.

3.4. FRB Host and Central Galaxy Properties

We characterize the physical properties of the FRB host galaxy and the nearby central galaxy using two complementary approaches: (1) nebular emission line diagnostics based on GTC/OSIRIS spectroscopy, and (2) stellar population synthesis modeling via spectral energy distribution (SED) fitting with **Prospector**. The methodology and detailed derivations of line ratios, $\text{H}\alpha$ -based star formation rates (SFRs), gas-phase metallicities, and Baldwin-Phillips-Terlevich (BPT) classifications are described in Appendix B, while the SED modeling is detailed in Appendix C. The key derived properties of the FRB 20240114A host galaxy and the central galaxy are summarized in Table 3. We also perform a BPT diagnostic analysis (see Appendix B) to assess nuclear activity in both galaxies, which reveals that both galaxies are actively star-forming with no signatures of AGN activity.

The FRB host is a dwarf galaxy ($\log(M/M_{\odot}) = 8.6$) exhibiting sub-solar gas-phase metallicity, $\log(Z/Z_{\odot}) = -0.46 \pm 0.17$, and an elevated SFR of $0.06 M_{\odot} \text{ yr}^{-1}$, which is in excellent agreement with the dust-corrected $\text{H}\alpha$ estimate. In contrast, the central galaxy is more massive ($\log(M/M_{\odot}) = 9.8$), more metal-rich ($\log(Z/Z_{\odot}) = -0.25 \pm 0.19$), and forms stars at $\sim 0.52 M_{\odot} \text{ yr}^{-1}$. Moreover, both galaxies are classified as star-forming based on their specific SFRs (Salim et al. 2007). We note that our derived host properties are broadly consistent with Chen et al. (2025). However,

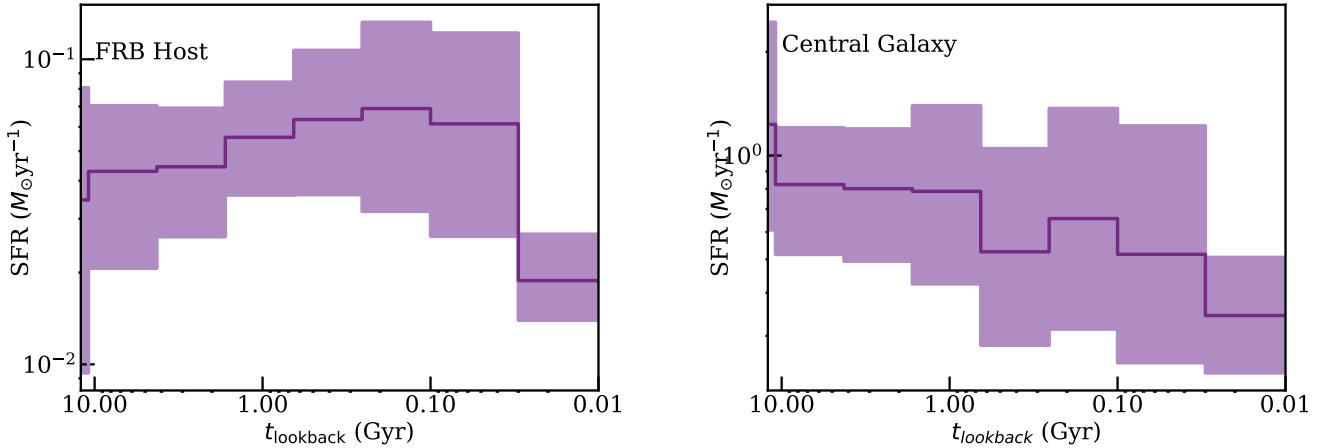


Figure 5. Nonparametric star-formation histories. The left panel shows the SFH of the FRB host galaxy, and the right panel that of the central companion, both reconstructed with *Prospector* (see §3.4 and Appendix C). Solid lines indicate the median SFR in each time bin; shaded envelopes mark the 16th–84th percentile credible intervals.

our SFR is approximately 6 times smaller than what [Bruni et al. \(2025\)](#) estimated, who report an extinction-corrected SFR of $0.36 M_{\odot} \text{ yr}^{-1}$ driven by an anomalously high Balmer decrement ($H\alpha/H\beta \simeq 8$). We attribute their elevated ratio to differential slit losses and atmospheric refraction, as both our data and that of [Chen et al. \(2025\)](#) — which used wider slits — yield $H\alpha/H\beta \sim 2.9$, indicating minimal nebular extinction.

Our nonparametric SFHs (Figure 5) further reveal that the FRB host experienced a burst of star formation ≈ 30 – 50 Myr ago, analogous to those seen in the Magellanic Clouds ([Harris & Zaritsky 2009](#)). In contrast, the central galaxy displays a smoothly declining SFR, akin to the Milky Way’s evolutionary history ([Massana et al. 2022](#)). Together, these analyses paint a coherent picture of two relatively young, gas-rich systems. Building on these individual characterizations, we now assess the evidence for their association as a satellite-central system in §3.5.

3.5. Assessing the Satellite Association of the FRB Host

In this section, we evaluate the prospects of the FRB host and the central galaxy forming a satellite-central system. The angular separation between the two galaxies ($35.5''$) translates to a projected galactocentric distance $R_{\text{proj}} \approx 85$ kpc at $z = 0.1300$.

From Table 3, the central galaxy’s stellar mass is $\approx 6.8 \times 10^9 M_{\odot}$. This implies a host halo mass $M_{\text{halo}} \approx 3 \times 10^{11} M_{\odot}$, derived using the stellar-to-halo mass relation from [Moster et al. \(2010\)](#). Using this halo mass, the virial radius (R_{vir}) and virial velocity (V_{vir}) are calculated from standard definitions. The virial radius, defined as the radius where the average halo density is 200 times the critical density (ρ_{crit}) of the Universe at the central galaxy’s redshift, is

$$R_{\text{vir}} = \left(\frac{3M_{\text{halo}}}{4\pi\Delta_{\text{vir}}\rho_{\text{crit}}(z)} \right)^{1/3} \approx 132 \text{ kpc}, \quad (4)$$

where $\Delta_{\text{vir}} = 200$. The corresponding virial velocity is

$$V_{\text{vir}} = \sqrt{\frac{GM_{\text{halo}}}{R_{\text{vir}}}} \approx 98 \text{ km s}^{-1}. \quad (5)$$

The escape velocity, relevant for a bound orbit, is estimated as $v_{\text{esc}} \approx \sqrt{2}V_{\text{vir}} \approx 139 \text{ km s}^{-1}$. The FRB host and its putative central companion share the same systemic redshift, $z = 0.1300$ (Table 3). Therefore, to calculate their line-of-sight separation, we use the estimated uncertainty in the FRB host redshift, i.e., $\Delta z = 0.0002$. This corresponds to a line-of-sight velocity offset relative to the central galaxy of $v_{\parallel} = c\Delta z \approx 60 \text{ km s}^{-1}$.

The observed projected separation ($R_{\text{proj}} \approx 85$ kpc) is well within the central galaxy’s virial radius ($R_{\text{vir}} \approx 132$ kpc), corresponding to $R_{\text{proj}}/R_{\text{vir}} \approx 0.64$. Crucially, the observed line-of-sight velocity offset ($v_{\parallel} = 60 \text{ km s}^{-1}$) is significantly less than the estimated escape velocity ($v_{\text{esc}} \approx 139 \text{ km s}^{-1}$). While we only observe the line-of-sight component, this

indicates that the FRB host galaxy’s kinematics are fully consistent with bound orbital motion within the central galaxy’s gravitational potential. It is noted that residual velocity differences may stem from intrinsic peculiar motions of satellites (up to a few hundred km s^{-1}), measurement uncertainties in systemic redshift (typically $\sim 20\text{--}30 \text{ km s}^{-1}$), or minor contributions from gravitational redshift or large-scale flows. These effects are comparable to the escape velocity threshold. Therefore, even if we use $\Delta z = 0.0004$, our conclusions do not change.

Next, we examine the specific phase-space coordinates of the FRB host ($R_{\text{proj}}/R_{\text{vir}} \approx 0.64$ and $v_{\parallel}/V_{\text{vir}} \approx 0.61$) to determine their prevalence within known satellite populations and cosmological simulations. Empirical observations of satellite galaxies in the Local Group provide crucial context. For instance, the Sculptor dwarf spheroidal galaxy, a classical Milky Way satellite, is located at a projected radius of $R_{\text{proj}} \approx 85 \text{ kpc}$ ($R_{\text{proj}}/R_{\text{vir}} \approx 0.43$) with a line-of-sight velocity of $\sim 110 \text{ km/s}$ (Bettinelli et al. 2019). This velocity translates to $v_{\parallel}/V_{\text{vir}} \approx 0.61$ relative to a Milky Way virial velocity of $\sim 180 \text{ km/s}$ (Dehnen et al. 2006), demonstrating kinematics consistent with the FRB host’s observed velocity ratio. More importantly, Sculptor represents a typical, relatively undisturbed satellite in the intermediate halo, exhibiting kinematics that are common rather than extreme. Furthermore, high-resolution ΛCDM cosmological simulations (e.g., IllustrisTNG: Pillepich et al. 2018; EAGLE: Schaller et al. 2015; AQUARIUS: Springel et al. 2008) provide a robust statistical framework. These simulations consistently show that a significant fraction, typically $\sim 30\text{--}50\%$ or more, of gravitationally bound subhalos at comparable projected radii ($0.6\text{--}0.7 R_{\text{vir}}$) exhibit line-of-sight velocities within the range of $0.5\text{--}0.7\times$ the host’s characteristic velocity scale (e.g., Han et al. 2016; Wetzel et al. 2014). This population naturally arises from subhalos on a wide range of orbits, including more typical, moderately eccentric paths that constitute the majority of the satellite population. The observed phase-space location of the FRB host, therefore, places it firmly within the statistically common distribution of satellite galaxies, rather than in an extreme or anomalous kinematic regime.

Finally, we quantify the probability that the FRB host galaxy is an unrelated field galaxy (an ‘interloper’) by chance alignment. We define a redshift-space cylinder using the central galaxy’s virial properties. The cylinder’s projected radius is $R_{\text{vir}} = 0.132 \text{ Mpc}$. For the line-of-sight depth, we consider a window of $\pm 3\sigma_{\text{halo}}$, where $\sigma_{\text{halo}} \approx 0.8 \times V_{\text{vir}}$. With an updated $V_{\text{vir}} = 98 \text{ km/s}$, this results in $\sigma_{\text{halo}} \approx 78.4 \text{ km/s}$, and a total velocity window of $2 \times 3\sigma_{\text{halo}} \approx 470 \text{ km/s}$. The redshift-space depth of this cylinder is therefore $\Delta Z = (470 \text{ km/s})/H(z) \approx 6.5 \text{ Mpc}$. The volume of this redshift-space cylinder is $V_z = \pi R_{\text{vir}}^2 \times \Delta Z \approx 0.36 \text{ Mpc}^3$. Using a cosmic number density for dwarf galaxies with stellar masses comparable to or more massive than the FRB host ($M_{\text{stellar}} = 10^{8.3} M_{\odot}$), $n_g \approx 0.0075 \text{ Mpc}^{-3}$ (Baldry et al. 2008), the expected number of random interlopers in this volume is $N = n_g \times V_z \approx 0.0027$. Assuming Poisson statistics, the probability of detecting one or more such field galaxies by chance is $P(X \geq 1) = 1 - e^{-N} \approx 0.0027$.

In summary, the FRB host galaxy’s position and velocity relative to the central galaxy are kinematically consistent with a bound orbit, with its line-of-sight velocity well below the estimated escape velocity. Its phase-space location is statistically common among observed and simulated satellite populations. Furthermore, the quantitative assessment of the chance alignment hypothesis demonstrates a very low probability of the FRB host being an unrelated field galaxy. Synthesizing these lines of evidence, we conclude that the FRB host galaxy is likely to be a gravitationally bound satellite of the central galaxy.

Finally, we note that the relative properties of the two galaxies are consistent with expectations for a satellite-central system. The FRB host has a stellar mass over one-tenth that of the central galaxy, in line with typical satellite-central mass ratios in group environments (Behroozi et al. 2013; Weisz et al. 2015). It is also $\sim 0.25 \text{ dex}$ more metal-poor, consistent with the mass-metallicity relation (Gallazzi et al. 2005) and with metallicity differences observed in star-forming satellite-central pairs (Pasquali et al. 2012). Furthermore, the host’s low metallicity and active star formation resemble those of the Magellanic Clouds, a well-known gas-rich companion to the Milky Way. While the analogy is illustrative, we note that the central galaxy in our system is less massive than the Milky Way, suggesting that the FRB host-central pair resides in a lower-mass group regime.

4. DISCUSSION AND CONCLUSION

In this work, we present the milliarcsecond-precision EVN localization of FRB 20240114A ($\sim 90 \times 30 \text{ mas}$, $1\text{-}\sigma$), representing a several-hundred-fold improvement in sky-area uncertainty over the previous MeerKAT position (Tian et al. 2024b). At $z = 0.1300$, this corresponds to $\lesssim 100 \text{ pc}$ precision, firmly placing the FRB source 0.5 kpc ($0.6 R_e$) from its dwarf host nucleus. Although ground-based imaging cannot yet resolve its immediate environment, space-based instruments such as *Hubble Space Telescope* and *James Webb Space Telescope*, or high-resolution ALMA observations, could search for coincident star clusters or giant molecular clouds, thereby discriminating between young magnetar and

compact merger progenitors. We also confirm positional agreement (within 13 mas) with the PRS candidate presented by [Bruni et al. \(2025\)](#), but do not comment further on the nature of the PRS using our EVN data because they do not reach a sufficient depth or calibration accuracy.

Using spectroscopic observations from the GTC, we estimate the redshift and physical properties of the FRB 20240114A host galaxy. The FRB host is a dwarf star-forming galaxy at $z = 0.1300 \pm 0.0002$, which closely resembles the Small Magellanic Cloud in stellar mass ($\approx 4 \times 10^8 M_\odot$), metallicity ($12 + \log([O/H]) \approx 8.2$), SFR ($\approx 0.06 M_\odot \text{ yr}^{-1}$), and size ([Montes et al. 2024](#)). This characterization adds to a growing number of hyperactive FRBs, including FRB 20121102A ([Chatterjee et al. 2017](#); [Tendulkar et al. 2017](#)) and FRB 20190520B ([Niu et al. 2022](#)), that are found in dwarf galaxies similar to FRB 20240114A’s host. It is noteworthy that most hyperactive repeaters — including our source, FRB 20121102A, and FRB 20190520B — now originate from dwarfs with stellar masses $\lesssim 10^9 M_\odot$ (or luminosities $\lesssim 0.01 L^*$), a fraction significantly higher than the few percent ($\lesssim 5\%$) of the Universe’s total stellar mass found in such galaxies (e.g., [Baldry et al. 2012](#)). This disproportionate association can be explained if FRBs track star-formation over stellar mass ([Loudas et al. 2025](#)), which can also help explain the observed prevalence of dwarf hosts. The association of some FRBs with dwarf galaxies may also be related to the typically low-metallicity environments found in such systems, which are conducive to the growth of high-mass stars. For example, [Bassa et al. \(2017\)](#) found the FRB 20121102A host to have a metallicity of $12 + \log([O/H]) = 8.0 \pm 0.1$.

Our DM budget analysis for FRB 20240114A indicates that the dominant contribution to the observed dispersion measure likely arises from the foreground halo term (DM_{halo}). This finding has significant implications, as this component was not explicitly modeled in previous studies (e.g., [Tian et al. 2024b](#); [Chen et al. 2025](#)), leading to the unusually high DM of this FRB being considered a conundrum. A similar conclusion was reached for FRB 20190520B ([Lee et al. 2023](#)), where the foreground halo contribution to the FRB DM is substantial, suggesting that such a dominant foreground contribution may be a recurring feature, particularly for FRBs with unusually high extragalactic DM. If this trend persists, it would support the use of foreground galaxy counts as empirical proxies for estimating the IGM contribution ([Hsu et al. 2025](#)). This would not only improve our understanding of FRB environments but also enhance the precision of FRB-based cosmological measurements. Our result thus underscores the value of incorporating foreground information into FRB analyses, both for characterizing local environments and for unlocking the full potential of FRBs as cosmological probes.

A major discovery in this work is the identification of the FRB host as a satellite of a more massive, star-forming spiral galaxy, DESI J212740.488+041911.64. Our GTC spectroscopic follow-up analysis confirms that this central galaxy is at the same redshift as the FRB host, with a projected offset of ~ 85 kpc. Until now, securely localized FRB hosts have been either isolated dwarfs or isolated spirals/ellipticals. Our system represents the first established case of an FRB residing in a gravitationally bound dwarf-central pair, adding a wholly new class of environment for FRB engines. This observed satellite-central configuration, with an SMC-like dwarf host galaxy and a more massive central galaxy, mirrors the Small Magellanic Cloud–Milky Way system, albeit at a lower overall mass scale as the central galaxy is significantly less massive than the Milky Way. Even without clear tidal features noted in our current analysis, this pair invites targeted searches for interaction-driven starbursts, which are often seen in satellite-central systems. Such observations could test whether tidal encounters play a significant role in creating FRB progenitors, as some authors have proposed (e.g., [Kaur et al. 2022](#)).

This satellite association also has profound implications for future FRB host identification and characterization. Other known repeating FRBs have shown offsets of tens of kpc from massive galaxies, such as FRB 20200120E ([Bhardwaj et al. 2021a](#)), associated with a globular cluster within M81 ([Kirsten et al. 2022](#)), and FRB 20240209A, offset from a quiescent elliptical galaxy ([Shah et al. 2025](#); [Eftekhari et al. 2025](#)). The case of FRB 20190208A ([Hewitt et al. 2024b](#)), a repeating FRB whose host appears to be an exceptionally low-luminosity ($\sim 0.001\text{--}0.05 L^*$) dwarf galaxy offset by $\sim 10''$ from two more massive galaxies, further illustrates this. While the lack of a redshift determination for the ultra-faint host of FRB 20190208A currently precludes a definitive association, it is likely that in the future, some FRBs will appear host-less but will be tens of arcseconds, in projection, from a massive galaxy. The latter may well prove to be the central galaxy of an as-yet unseen low-luminosity satellite host. A faint satellite like the host of FRB 20240114A (or FRB 20190208A) would be invisible in standard follow-up at modest redshifts in archival datasets, thus masquerading as “hostless” or appearing to show a high offset from the closest galaxy in the survey. The commonly used PATH algorithm ([Aggarwal et al. 2021](#)) might even assign a low probability of association to the central galaxy, given a precise and well-offset radio localization. Recognizing and systematically identifying this

population of faint satellite hosts could substantially revise redshift and energetics distributions for “hostless” FRBs, highlighting the need for deeper optical observations around seemingly isolated FRBs.

In conclusion, our precise localization of FRB 20240114A combined with comprehensive spectroscopic and photometric analyses reveals a complex and unique environment for a repeating FRB. We’ve confirmed its location within a dwarf galaxy, shed light on the potentially dominant role of foreground halo DM, and, most notably, established its first-of-its-kind satellite association within a larger galactic system. This discovery expands the known diversity of FRB host environments and underscores the importance of multi-wavelength follow-up and careful consideration of intervening structures for a complete understanding of FRB progenitors and their utility as cosmological probes. The 0.5-kpc offset of FRB 20240114A from its dwarf host’s center is also consistent with a source that could be the product of a binary merger (Nugent et al. 2024), although detailed space-based observations are needed to confirm the local star-formation environment. This work opens new avenues for investigating the formation channels of FRBs, particularly in interacting galactic systems, and redefines our perspective on “hostless” FRBs.

5. ACKNOWLEDGMENTS

We thank Vishwangi Shah, Alexa Gordon, and Wen-fai Fong for useful conversations. The European VLBI Network is a joint facility of independent European, African, Asian, and North American radio astronomy institutes. Scientific results from data presented in this publication are derived from the following EVN project code(s): EK056. This work is based in part on observations carried out using the 32-m radio telescope operated by the Institute of Astronomy of the Nicolaus Copernicus University in Toruń (Poland) and supported by a Polish Ministry of Science and Higher Education SpUB grant. The Onsala Space Observatory national research infrastructure is funded through Swedish Research Council grant No. 2017-00648. e-MERLIN is a National Facility operated by the University of Manchester at Jodrell Bank Observatory on behalf of STFC, part of UK Research and Innovation. This research has made use of the NASA/IPAC Extragalactic Database (NED), which is operated by the Jet Propulsion Laboratory, California Institute of Technology, under contract with the National Aeronautics and Space Administration. This research used data obtained with the Dark Energy Spectroscopic Instrument (DESI). DESI construction and operations is managed by the Lawrence Berkeley National Laboratory. This material is based upon work supported by the U.S. Department of Energy, Office of Science, Office of High-Energy Physics, under Contract No. DE-AC02-05CH11231, and by the National Energy Research Scientific Computing Center, a DOE Office of Science User Facility under the same contract. Additional support for DESI was provided by the U.S. National Science Foundation (NSF), Division of Astronomical Sciences under Contract No. AST-0950945 to the NSF’s National Optical-Infrared Astronomy Research Laboratory; the Science and Technology Facilities Council of the United Kingdom; the Gordon and Betty Moore Foundation; the Heising-Simons Foundation; the French Alternative Energies and Atomic Energy Commission (CEA); the National Council of Humanities, Science and Technology of Mexico (CONAHCYT); the Ministry of Science and Innovation of Spain (MICINN), and by the DESI Member Institutions: www.desi.lbl.gov/collaborating-institutions. The DESI collaboration is honored to be permitted to conduct scientific research on I’oligam Du’ag (Kitt Peak), a mountain with particular significance to the Tohono O’odham Nation. Any opinions, findings, and conclusions or recommendations expressed in this material are those of the author(s) and do not necessarily reflect the views of the U.S. National Science Foundation, the U.S. Department of Energy, or any of the listed funding agencies. M.B. is a McWilliams fellow and an International Astronomical Union Gruber fellow. M.B. also receives support from two McWilliams seed grants. M.P.S., J.W.T.H. and the AstroFlash research group acknowledge support from a Canada Excellence Research Chair in Transient Astrophysics (CERC-2022-00009); an Advanced Grant from the European Research Council (ERC) under the European Union’s Horizon 2020 research and innovation programme (‘EuroFlash’; Grant agreement No. 101098079); and an NWO-Vici grant (‘AstroFlash’; VI.C.192.045). A.GdP. is partly supported by grant PID2022-138621NB-I00 funded by MCIN/AEI/10.13039/501100011033 and ‘ERDF A way of making Europe’. S.B. is supported by a Dutch Research Council (NWO) Veni Fellowship (VI.Veni.212.058). B.M. acknowledges financial support from the State Agency for Research of the Spanish Ministry of Science and Innovation, and FEDER, UE, under grant PID2022-136828NB-C41/MICIU/AEI/10.13039/501100011033, and through the Unit of Excellence María de Maeztu 2020–2023 award to the Institute of Cosmos Sciences (CEX2019-000918-M). A.K. acknowledges the DGAPA-PAPIIT grant IA105024. F.K. acknowledges support from Onsala Space Observatory for the provisioning of its facilities/observational support. M.P.G. acknowledges the support of the Anton Pannekoek Institute for Astronomy during his visit to the University of Amsterdam. K.N. is an MIT Kavli Fellow. N.W. is supported by the National Natural Science Foundation of China (Nos. 12288102 and 12041304).

6. DATA AVAILABILITY

Uncalibrated visibilities of FRB 20240114A and its calibration sources can be downloaded from the JIVE/EVN archive, <https://archive.jive.eu>, under project codes EK056A and EK056B. Filterbank files, calibrated burst visibilities, dirty maps fits files and the scripts that made Figures 1, 2, 6 and 7, and Table 1 can be accessed in our Zenodo reproduction package: *Zenodo DOI will be made public once the paper is accepted*. The burst baseband data (i.e. raw voltages) and the GTC spectroscopy data presented in this paper will be made available by the authors upon reasonable request.

Facilities: EVN, OSIRIS+(GTC)

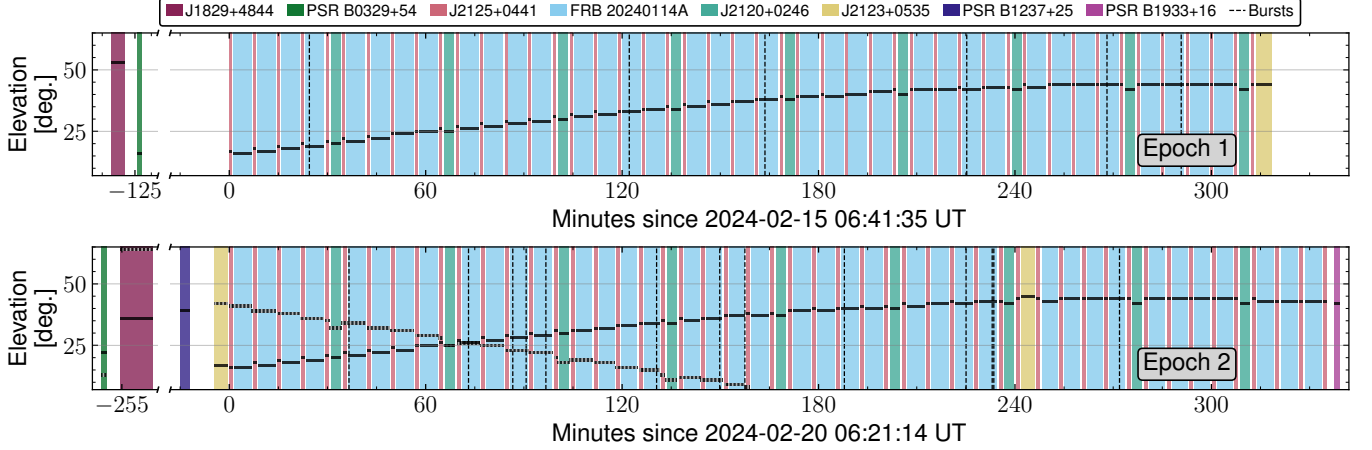


Figure 6. Observational timeline and calibration strategy for Epoch 1 (top panel; PR318A/EK056A) and Epoch 2 (bottom panel; PR319A/EK056B). The ~ 6 minute target scans on FRB 20240114A are interleaved with ~ 2 minute scans on the phase-calibrator J2125+0441. Roughly twice per hour the check-source, J2120+0246, was observed for ~ 3.5 minutes per scan to verify the astrometric calibration. Other sources include J1829+4844 and J2123+0535, which are used as fringe finders and bandpass calibrators, and various pulsars to test the data quality, frequency setup and the burst-search pipeline. The solid horizontal black bars indicate the source elevation for the Effelsberg telescope (Germany) and the horizontal black-grey dashed bars indicate the same for the Tianma telescope (China). Vertical black dashed lines indicate the arrival times of the bursts. Vertical white bars indicate that the telescopes are slewing (slewing/on-source times are shown for Effelsberg, which is the slowest slewing antenna in the array).

Software: SFXC (Keimpema et al. 2015), CASA (McMullin et al. 2007), Heimdall (Barsdell & Jameson 2024), DSPSR (van Straten & Bailes 2011), FETCH (Agarwal et al. 2020), AIPS (Greisen 2003), DIFMAP (Shepherd 1997), Prospector (Leja et al. 2017; Johnson et al. 2021).

APPENDIX

A. DM CONTRIBUTION OF THE INTERSECTING FOREGROUND GALAXIES

This section details our methodology for identifying foreground galaxies whose halos intersect the FRB sightline and contribute to its observed DM. We begin by querying the DESI Legacy Imaging Survey photometric redshift catalog (Zou et al. 2019) within 0.5° of the EVN-derived FRB localization. To select relevant foreground galaxies, we apply two primary criteria:

1. The mean photometric redshift $\langle z \rangle$ must satisfy $\langle z \rangle - 2\sigma_z \leq 0.1300$, where 0.1300 is the spectroscopic redshift of the FRB host galaxy and σ_z is the uncertainty on $\langle z \rangle$ reported in the DESI Legacy Imaging Survey photometric redshift catalog.
2. The angular offset θ_{offset} between the FRB and the galaxy centroid, normalized by the effective radius R_{eff} , must satisfy $\theta_{\text{offset}}/R_{\text{eff}} > 0.018$. This ratio, hereafter referred to as the intersection ratio (or int. ratio in Table 5), uses 0.018 as the empirically determined stellar-to-halo-radius ratio (SRHR) at $z \leq 0.1$ (Somerville et al. 2018), ensuring the FRB’s projected offset falls within the foreground galaxy’s virial radius (R_{200}). For more detail, refer §3.2.

Excluding the FRB host and DESI J212740.488+041911.64 — i.e., the central galaxy — these criteria yield seven candidate foreground galaxies. Their properties are summarized in Table 5, and their DESI color cutouts are shown in Figure 8. Note that Galaxy 1 in Figure 8 corresponds to the central galaxy, and its properties are discussed in §3.4.

We now describe the formalism used to estimate $\text{DM}_{\text{fg halo}}$ for the intersecting galaxy. For each candidate, we first estimate the stellar mass using the empirically derived relation by Taylor et al. (2011):

$$\log_{10}(M_*/M_\odot) = -0.68 + 0.70(g - i) - 0.4M_i, \quad (\text{A1})$$

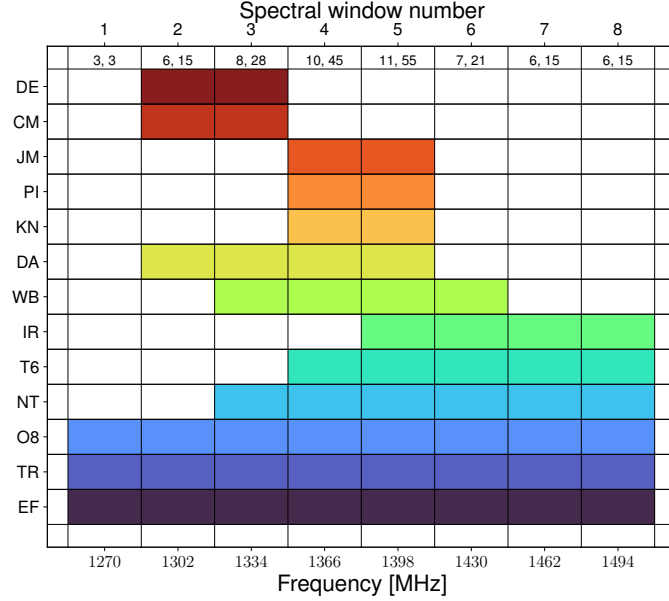


Figure 7. Observed frequencies per antenna. Every antenna recorded at least two 32-MHz spectral windows. The numbers below the spectral window number indicate the number of antennas, n , that recorded that spectral window and the corresponding number of unique baselines, $\frac{1}{2}n(n-1)$.

where M_i is the rest-frame i -band AB absolute magnitude ($M_{i,\odot} = 4.58$), derived from SDSS photometric data in g and i bands (Abdurro'uf et al. 2022). The stellar mass is then inverted using the Moster et al. (2010) stellar-to-halo mass relation to obtain the halo mass (M_{halo}). At the galaxy's redshift z , we compute the virial radius using Equation 4 and determine the Navarro-Frenk-White (NFW) concentration c using the Dutton & Macciò (2014) concentration-mass relation.

We then model the circumgalactic medium (CGM) gas of the galaxies using the modified NFW halo profile from Prochaska & Zheng (2019):

$$\rho(r) = \frac{f_{\text{gas}} f_b \rho_0}{y^{1-\alpha} (y_0 + y)^{2+\alpha}}, \quad y = c \frac{r}{R_{200}}, \quad (\text{A2})$$

where α and y_0 describe the inner and outer slopes, $f_b = \Omega_b/\Omega_m \approx 0.16$ is the cosmic baryon fraction, and $f_{\text{gas}} = 0.75$ is the fraction of baryons in the CGM gas phase. The central density ρ_0 is given by:

$$\rho_0 = \frac{200 \rho_c(z)}{3} \frac{c^3}{\ln(1+c) - c/(1+c)}. \quad (\text{A3})$$

Following the prescription by Prochaska & Zheng (2019), we use Equation A3 to estimate the free-electron density profile $n_e(r)$ and subsequently calculate DM_{halo} by numerically integrating $n_e(r)$ along each FRB sightline, with the measured angular offset setting the impact parameter.

Among the seven galaxies, spectroscopic redshifts for Galaxies 4, 6, 7, and 8 are available from NED (Mazzarella & NED Team 2007). Using this redshift information and the formalism described above, we estimate their $\text{DM}_{\text{fg halo}}$ contributions. Notably, the projected offsets of Galaxies 4 and 8 are found to be beyond their virial radii, resulting in $\text{DM}_{\text{fg halo}} = 0$ for these two galaxies. The estimated $\text{DM}_{\text{fg halo}}$ for Galaxies 6 and 7 are reported in Table 5. For the remaining three galaxies (Galaxies 2, 3, and 5) that lack spectroscopic redshifts but satisfy our first selection criterion (despite $z_{\text{phot}} > 0.13$), we employ a Monte Carlo sampling approach to estimate their halo contributions. We sample the redshift 100,000 times from a Gaussian prior $\mathcal{N}(\langle z \rangle, \sigma_z^2)$. Samples with $z > 0.1300$ are excluded, effectively creating a truncated Gaussian distribution with a maximum at $z = 0.1300$. We then estimate $\text{DM}_{\text{fg halo}}$ for each redshift value. The mean of these estimated $\text{DM}_{\text{fg halo}}$ values is reported in Table 5. Summing all seven contributions yields a total observer-frame $\text{DM}_{\text{fg halo}} = 124 \text{ pc cm}^{-3}$. If we include the DM contribution from the central galaxy's halo, estimated to be 11 pc cm^{-3} based on its halo mass of $\approx 3 \times 10^{11} M_{\odot}$ (as computed in §3.5) and the formalism described above, the total becomes 135 pc cm^{-3} . As evident from Table 5, Galaxy 6 contributes most significantly to the $\text{DM}_{\text{fg halo}}$ estimate;

Table 4. Observational setup.

Telescope	Abbr. ^a	SEFD ^b	ν ^c	$\Delta\nu$ ^c	Diameter ^b
		[Jy]	[MHz]	[MHz]	[m]
Effelsberg	EF	19	1254–1510	256	100
Westerbork ^d	WB	420	1318–1446	128	25
Toruń	TR	250	1254–1510	256	32
Noto ^e	NT	740	1318–1510	192	32
Onsala 25-m	O8	310	1254–1510	256	25
Irbene	IR	700	1382–1510	256	32
Tianma ^f	T6	39	1350–1510	256	65
Jodrell Bank ^g	JM	325	1350–1414	64	38x25
Cambridge ^h	CM	200	1286–1350	64	32
Darnhall	DA	450	1286–1414	128	25
Defford	DE	350	1286–1350	64	25
Knockin ^h	KN	425	1350–1414	64	25
Pickmere ^h	PI	400	1350–1414	64	25

^a Telescope abbreviation as used in Figure 7.

^b From the EVN status table^a.

^c The frequency range ν and the bandwidth $\Delta\nu$ do not account for flagged band edges.

^d Single dish, Westerbork RT-1.

^e Recorded data up to 1574 MHz, but data beyond 1510 MHz is not correlated.

^f Only participated in Epoch 2. Has a linear polarization receiver and the data is converted to a circular basis before correlation.

^g Jodrell Bank Mark II.

^h Due to a technical issue these stations only recorded right circular polarization (both epochs).

^a <https://www.evlbi.org/sites/default/files/shared/EVNstatus.txt>

this galaxy is a bright and massive member of the galaxy cluster J212719.9+042225 (Wen & Han 2024). To account for systematic uncertainties inherent in the color-stellar mass calibration, halo mass inversion, concentration relation, and profile parameters, we adopt a conservative 50% one-sigma scatter on our final $\text{DM}_{\text{fg halo}}$ estimates, consistent with other similar studies (e.g., see Simha et al. 2023; Anna-Thomas et al. 2025). This leads to a total observer-frame $\text{DM}_{\text{fg halo}} = 135 \pm 68 \text{ pc cm}^{-3}$.

Finally, to ensure no local Universe galaxies with large angular virial radii were missed by our initial 0.5° search, we cross-referenced our findings with the Heraklion Extragalactic Catalogue (HECATE; Kovlakas et al. 2021), which compiles nearby galaxies within $\sim 200 \text{ Mpc}$. Stellar masses from HECATE were converted into halo masses using the stellar-to-halo mass relation of Moster et al. (2010), and corresponding virial radii were computed. A comprehensive search within 30° of the FRB revealed no additional foreground galaxies.

B. NEBULAR EMISSION LINE ANALYSIS OF THE FRB HOST AND THE CENTRAL GALAXY

In this section, we describe the methodology used to derive various physical properties of the FRB host and the central galaxy, namely $\text{H}\alpha$ luminosities and $\text{H}\alpha$ -assisted SFR, nebular metallicity, and BPT diagnostics, using the emission lines modeled and calibrated from the GTC spectra of the FRB and the central galaxy. The procedure used to identify and calibrate the flux densities of the emission lines reported in Table 2 is described in §3.3. Besides the observed (f_{data} , $f_{1\text{G}}$) and extinction-corrected ($f_{\text{data,c}}$, $f_{1\text{G,c}}$) fluxes and errors (δ), either measured directly from the spectra or after fitting single-Gaussian and their errors, respectively, we also provide in this table the corresponding equivalent widths (EW). The extinction-corrected line ratios are given in Table 6.

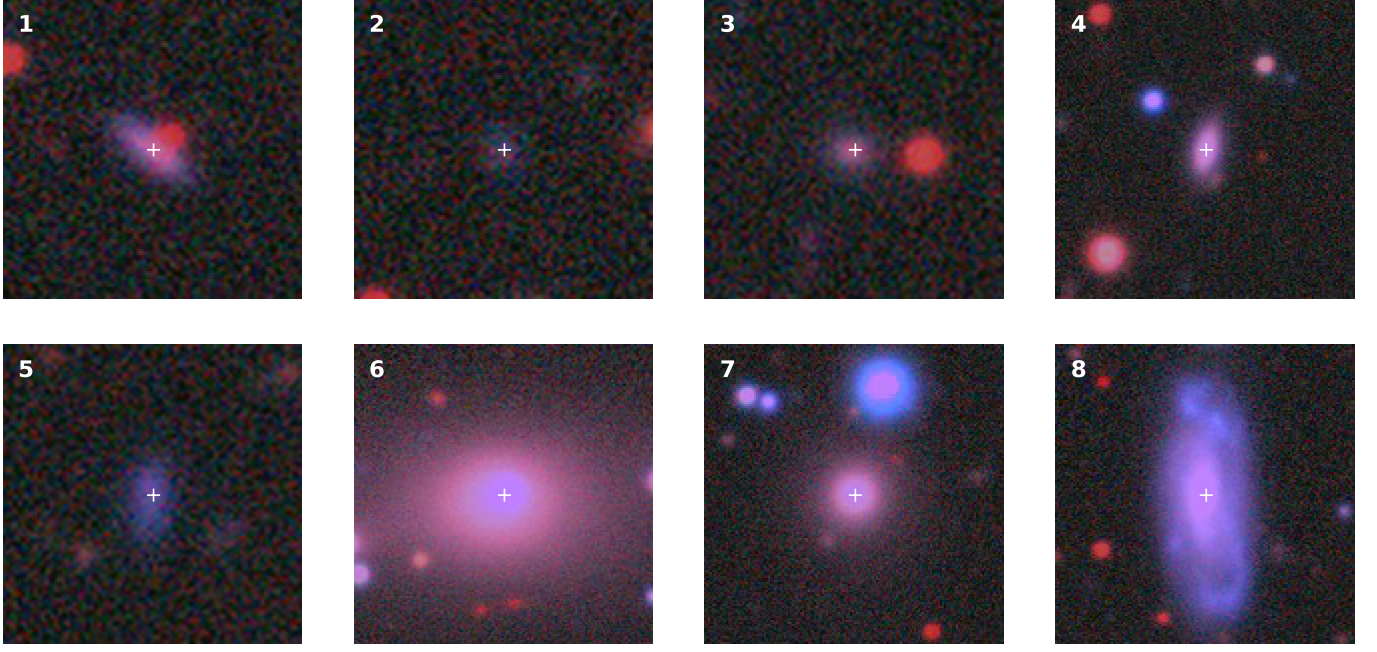


Figure 8. RGB composite (R =DESI z -band, G =DESI r -band, B =DESI g -band) of the eight foreground galaxies whose halos intersect the FRB 20240114A sightline. Each $1.5' \times 1.5'$ panel is centered on the galaxy centroid (marked by a white cross) and is displayed at the same stretch for direct comparison. Galaxies are numbered in order of increasing angular separation from the FRB position, as listed in Table 5.

Table 5. Photometric and Redshift Properties of Galaxies Near FRB 20240114A.

No.	α^a	δ^a	r -mag (AB)	$\langle z \rangle$	σ_z	θ_{offset} (")	Int. Ratio	M_r (AB)	z_{spec}	$\text{DM}_{\text{fg halo}}$ (pc cm^{-3})
2	21 ^h 27 ^m 38 ^s .57	04°19'28".9	21.9	0.52	0.23	25.3	0.030	-	-	9
3	21 ^h 27 ^m 40 ^s .54	04°20'44".8	20.5	0.25	0.08	60.1	0.025	-	-	3
4	21 ^h 27 ^m 40 ^s .87	04°21'11".5	18.3	0.15	0.04	87.2	0.023	-19.7	0.090	0
5	21 ^h 27 ^m 42 ^s .82	04°18'34".5	20.6	0.18	0.15	84.1	0.022	-	-	3
6	21 ^h 27 ^m 25 ^s .44	04°22'46".5	15.2	0.05	0.02	281.2	0.019	-23.7	0.090	104
7	21 ^h 27 ^m 32 ^s .18	04°20'31".9	16.8	0.085	0.013	123.6	0.019	-21.2	0.090	5
8	21 ^h 27 ^m 06 ^s .58	04°19'01".5	15.8	0.031	0.012	499.3	0.018	-19.7	0.029	0

^a α and δ are provided in J2000.

Table 6. Extinction-corrected emission line ratios for the FRB host and the central galaxy.

Ratio	FRB host				Central galaxy			
	Best	16 %	50 %	84 %	Best	16 %	50 %	84 %
[O II]/[O III]	1.169	1.071	1.182	1.307	4.182	3.379	4.513	6.339
[O III]/H β	2.826	2.469	2.806	3.232	0.710	0.503	0.695	0.944
[N II]/H α	0.077	0.051	0.078	0.105	0.262	0.207	0.260	0.318
[S II]6717/H α	0.106	0.077	0.107	0.139	0.178	0.136	0.176	0.222

The line fluxes and ratios provided in Tables 2 and 6 are used to compute line ratios and H α luminosities. For the latter, we have adopted a luminosity distance of 614.6 Mpc based on the redshift of the object ($z = 0.1300$) and the

cosmological parameters from [Bennett et al. \(2014\)](#). To obtain the SFR of both targets, we made use of the calibration from [Kennicutt \(1998\)](#), for which an $H\alpha$ luminosity of $1.26 \times 10^{41} \text{ erg s}^{-1}$ is equivalent to a SFR of $1 M_{\odot} \text{ yr}^{-1}$.

The errors in the observed line fluxes were derived using the results from each individual fit to the continuum plus the corresponding line profile. The errors in the extinction-corrected line ratios, $H\alpha$ luminosities, and SFRs were computed starting from the errors in the observed line fluxes and then using a total of 1000 Monte Carlo realizations for each measurement. The error distributions for all these measurements were assumed to be Gaussian and uncorrelated. In Table 6, we provide the output 16–50–84% percentiles for the line ratios, as these are not perfectly Gaussian anymore. The same quantities in the case of the $H\alpha$ luminosities and SFRs are listed in Table 7. Thus, for the central galaxy ($A_V = 1.12$; Table 3), the dust-corrected SFR is $\text{SFR}_{\text{corr}} = (5.8_{-0.5}^{+2.6} \times 10^{-2} M_{\odot} \text{ yr}^{-1}) \times 10^{0.4 \times 1.12} = 0.16_{-0.01}^{+0.07} M_{\odot} \text{ yr}^{-1}$. For the FRB host ($A_V = 0.11$; Table 3), we similarly obtain $\text{SFR}_{\text{corr}} = (5.5_{-0.3}^{+0.4} \times 10^{-2} M_{\odot} \text{ yr}^{-1}) \times 10^{0.4 \times 0.11} = 0.061_{-0.003}^{+0.004} M_{\odot} \text{ yr}^{-1}$.

Next, we derive the gas-phase oxygen abundances for the FRB host and the central galaxy using the N2 and O3N2 empirical diagnostics calibrated by [Marino et al. \(2013\)](#). The N2 diagnostic is defined as

$$12 + \log(\text{O}/\text{H}) = 8.743 + 0.462 \times \log_{10}([\text{N II}]/\text{H}\alpha), \quad (\text{B4})$$

and the O3N2 diagnostic combines $[\text{O III}]/\text{H}\beta$ and $[\text{N II}]/\text{H}\alpha$ ratios as:

$$12 + \log(\text{O}/\text{H}) = 8.533 - 0.214 \times \log_{10}\left(\frac{[\text{O III}]/\text{H}\beta}{[\text{N II}]/\text{H}\alpha}\right). \quad (\text{B5})$$

The systematic uncertainties in these calibrations are 0.16 dex and 0.18 dex, respectively. We combine these in quadrature with the statistical uncertainties derived from the 16th and 84th percentile values of the line-ratio posteriors to report total uncertainties.

For the FRB host galaxy, we find:

$$12 + \log(\text{O}/\text{H}) = 8.23 \pm 0.17 \quad (\text{N2}), \quad \log(Z/Z_{\odot})_{\text{gas}} = -0.46 \pm 0.17,$$

$$12 + \log(\text{O}/\text{H}) = 8.20 \pm 0.19 \quad (\text{O3N2}), \quad \log(Z/Z_{\odot})_{\text{gas}} = -0.49 \pm 0.19.$$

For the central galaxy:

$$12 + \log(\text{O}/\text{H}) = 8.47 \pm 0.17 \quad (\text{N2}), \quad \log(Z/Z_{\odot})_{\text{gas}} = -0.22 \pm 0.17,$$

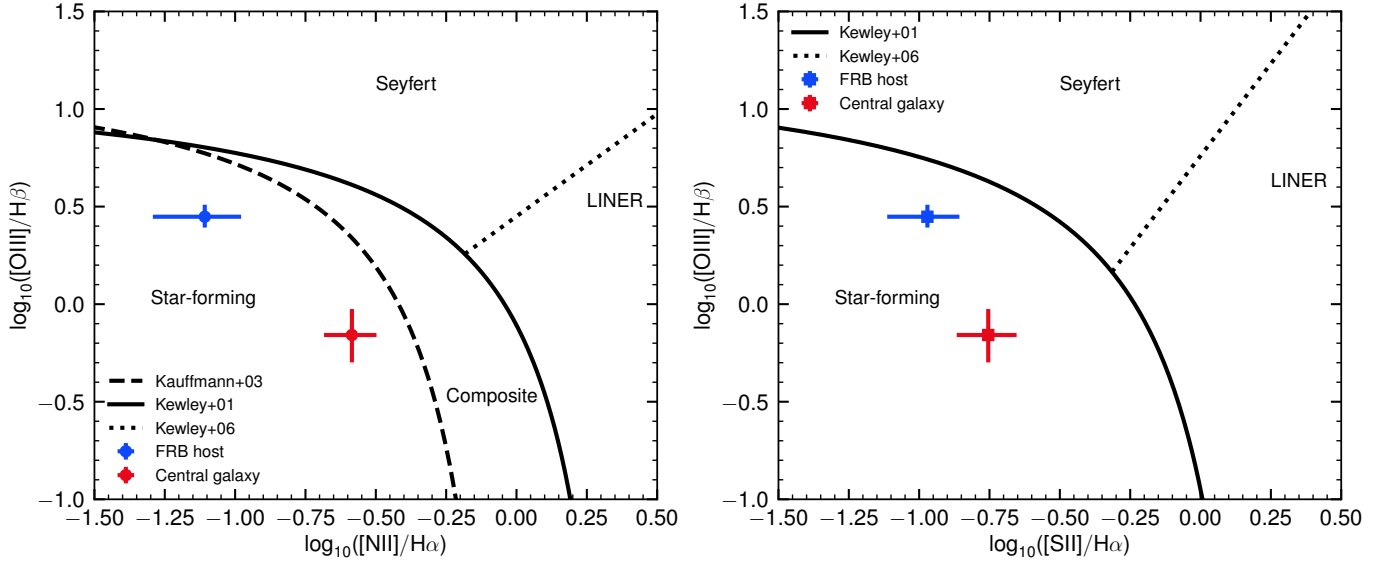
$$12 + \log(\text{O}/\text{H}) = 8.44 \pm 0.19 \quad (\text{O3N2}), \quad \log(Z/Z_{\odot})_{\text{gas}} = -0.25 \pm 0.19.$$

These values assume a solar oxygen abundance of $12 + \log(\text{O}/\text{H})_{\odot} = 8.69$ ([Asplund et al. 2009](#)). Table 3 lists the weighted-mean gas-phase metallicities for both galaxies, derived from the two independent estimates above.

To assess the dominant ionization mechanisms in both galaxies, we use the BPT diagnostic diagrams shown in Figure 9, employing the line ratios listed in Table 6. In the left panel, we plot $\log_{10}([\text{N II}]/\text{H}\alpha)$ versus $\log_{10}([\text{O III}]/\text{H}\beta)$, and in the right panel, $\log_{10}([\text{S II}]/\text{H}\alpha)$ versus $\log_{10}([\text{O III}]/\text{H}\beta)$. Both galaxies fall below the theoretical demarcation between AGN and star-forming galaxies from [Kewley et al. \(2001, Composite/AGN\)](#), the empirical star-forming sequence boundary from [Kauffmann et al. \(2003, SF/Composite\)](#), and the Seyfert-LINER division from [Kewley et al. \(2006\)](#). These positions confirm that the nebular emission in both galaxies is dominated by photoionization from young stars rather than by AGN activity, thus validating the use of H II-region calibrations for metallicity diagnostics. We also compute the $[\text{O III}]/[\text{O II}]$ line ratio, also known as the $O32$ ratio, which serves as an empirical proxy for the ionization parameter in H II regions (e.g., [Kewley et al. 2001; Nagao et al. 2006](#)). This ratio reflects the relative abundance of doubly ionized to singly ionized oxygen and is sensitive to both the hardness of the ionizing radiation and the geometry of the gas. For the FRB host galaxy, we find $\log_{10}([\text{O III}]/[\text{O II}]) = -0.07$, while the central galaxy shows a lower value of -0.62 . According to photoionization models (e.g., [Kewley et al. 2001](#)), values of $\log_{10}([\text{O III}]/[\text{O II}]) \gtrsim 0$ correspond to high ionization parameters (typical of extreme starbursts), whereas values between $-1 \lesssim \log_{10}([\text{O III}]/[\text{O II}]) \lesssim 0$ indicate moderate ionization levels characteristic of normal star-forming galaxies. Thus, both galaxies in our system lie within the expected range for moderately ionized H II regions, consistent with the BPT classification discussed above.

Table 7. $H\alpha$ luminosities and SFR values for the FRB host and the central galaxy.

Property	FRB host				Central galaxy			
	Best	16 %-perc.	50 %-perc.	84 %-perc.	Best	16 %-perc.	50 %-perc.	84 %-perc.
$H\beta_{\text{corr}} [10^{-17} \text{ erg s}^{-1} \text{ cm}^{-2}]$	6.08	5.66	6.23	6.93	5.41	5.57	6.25	7.99
$H\alpha_{\text{corr}} [10^{-17} \text{ erg s}^{-1} \text{ cm}^{-2}]$	15.3	14.6	15.4	16.4	15.5	14.8	16.2	23.4
$L(H\alpha_{\text{corr}}) [10^{39} \text{ erg s}^{-1}]$	6.89	6.58	6.94	7.41	7.00	6.67	7.34	10.6
$\text{SFR} [10^{-2} M_{\odot} \text{ yr}^{-1}]$	5.47	5.22	5.51	5.88	5.56	5.29	5.82	8.40

**Figure 9.** BPT diagnostic diagrams for the FRB host galaxy and its central galaxy. *Left panel:* $\log_{10}([\text{N II}]/\text{H}\alpha)$ vs. $\log_{10}([\text{O III}]/\text{H}\beta)$, with demarcation curves from (Kauffmann et al. 2003, SF/Composite), (Kewley et al. 2001, Composite/AGN), and the Seyfert-LINER division (Kewley et al. 2006). *Right panel:* $\log_{10}([\text{S II}]/\text{H}\alpha)$ vs. $\log_{10}([\text{O III}]/\text{H}\beta)$, showing the SF/AGN curve and the Seyfert-LINER boundary from Kewley et al. (2001) & Kewley et al. (2006), respectively. Error bars denote the median and 1- σ uncertainties derived from the 16th, 50th and 84th percentiles of each line ratio.

C. STELLAR POPULATION MODELING WITH PROSPECTOR

We model the stellar populations of the FRB host and its central galaxy using the `prospector` SED-fitting framework with the Flexible Stellar Population Synthesis (FSPS; Conroy et al. 2009; Conroy & Gunn 2010) library via `python-FSPS` (Foreman-Mackey et al. 2014). To fit both broadband photometry and GTC/OSIRIS spectroscopy simultaneously, we employ dynamic nested sampling as in Bhardwaj et al. (2021b) and Bhardwaj et al. (2024c). All data are first corrected for Milky Way extinction using the Fitzpatrick & Massa (2007) law (Fitzpatrick & Massa 2007) with $A_V = 0.18$ mag, and a 5% minimum uncertainty floor is applied to the photometry.

For the star-formation history (SFH) we use a nonparametric “continuity” model with eight time bins, imposing smoothness via a Student- t prior on the log-SFR ratios between adjacent bins (Bhardwaj et al. 2024c). We assume a Kroupa initial mass function (Kroupa 2001) and constrain stellar metallicities with a Gaussian prior based on the mass-metallicity relation of Gallazzi et al. (2005), using twice the observed scatter.

Dust attenuation follows the two-component model of Charlot & Fall (2000): young stars and nebular lines suffer a birth-cloud optical depth τ_1 , and all starlight is further reddened by a diffuse ISM optical depth τ_2 (Kriek & Conroy 2013). We fix τ_1 as a fraction of τ_2 and impose a Gaussian prior on τ_2 whose mean and width are scaled by the line-of-sight path length, $f_{\text{los}} = 1/\cos i$. For the FRB host, which is likely an irregular dwarf, we assume $i \approx 0^\circ$. For the central galaxy we adopt $i = 73^\circ$ from the SDSS exponential-fit axis ratio following Bhardwaj et al. (2024b). Thus a default face-on prior $\tau_2 \sim \mathcal{N}(0.3, 1.0)$ becomes $\tau_2 \sim \mathcal{N}(0.3 f_{\text{los}}, 1.0 f_{\text{los}})$.

We account for residual sky-line contamination with a pixel outlier model and include a two-component mid-infrared AGN contribution following [Leja et al. \(2018\)](#). All posteriors are sampled with 500 live points and a target sampling efficiency of 2%, and uncertainties are quoted as the 16th–84th percentile credible intervals.

Table 8. Broadband photometry used for SED modeling of the central galaxy and the FRB host.

Instrument	Filter	λ_{eff} [Å]	Magnitude [AB]
Central Galaxy			
SDSS ^a	u	3543	21.84 ± 0.33
SDSS ^a	g	4770	20.69 ± 0.06
SDSS ^a	r	6231	20.03 ± 0.06
SDSS ^a	i	7625	19.45 ± 0.06
SDSS ^a	z	9134	19.28 ± 0.09
WISE ^b	W1	33460	19.11 ± 0.06
WISE ^b	W2	45950	19.48 ± 0.09
FRB Host			
CFIS ^c	u (MegaCam)	3813	22.95 ± 0.12
SDSS ^a	g	4770	22.43 ± 0.13
SDSS ^a	r	6231	21.94 ± 0.11
SDSS ^a	i	7625	21.70 ± 0.16
SDSS ^a	z	9134	21.64 ± 0.45

^a Extinction corrected model magnitude from the SDSS DR12 catalog ([Alam & et al. 2015](#)).

^b From the unWISE catalog ([Schlafly et al. 2019](#)).

^c From the Canada-France Imaging Survey DR3 catalog (CFIS; [Ibata et al. 2017](#))

REFERENCES

- Abdurro’uf, Accetta, K., Aerts, C., et al. 2022, *ApJS*, 259, 35, doi: [10.3847/1538-4365/ac4414](#)
- Agarwal, D., Aggarwal, K., Burke-Spolaor, S., Lorimer, D. R., & Garver-Daniels, N. 2020, *MNRAS*, 497, 1661, doi: [10.1093/mnras/staa1856](#)
- Aggarwal, K., Budavári, T., Deller, A. T., et al. 2021, *ApJ*, 911, 95, doi: [10.3847/1538-4357/abe8d2](#)
- Alam, S., & et al. 2015, *ApJS*, 219, 12, doi: [10.1088/0067-0049/219/1/12](#)
- Allen, S. W., Schmidt, R. W., Allen, S. W., et al. 2004, *MNRAS*, 353, 457, doi: [10.1111/j.1365-2966.2004.07970.x](#)
- Andrew, S., & CHIME/FRB Collaboration. 2025, *The Astronomer’s Telegram*, 17114, 1
- Anna-Thomas, R., Law, C. J., Koch, E. W., et al. 2025, *arXiv e-prints*, arXiv:2503.02947, doi: [10.48550/arXiv.2503.02947](#)
- Asplund, M., Grevesse, N., Sauval, A. J., & Scott, P. 2009, *ARA&A*, 47, 481, doi: [10.1146/annurev.astro.46.060407.145222](#)
- Baldry, I. K., Glazebrook, K., & Driver, S. P. 2008, *MNRAS*, 388, 945, doi: [10.1111/j.1365-2966.2008.13600.x](#)
- Baldry, I. K., Driver, S. P., Loveday, J., et al. 2012, *MNRAS*, 421, 621, doi: [10.1111/j.1365-2966.2012.20340.x](#)
- Baptista, J., Prochaska, J. X., Mannings, A. G., et al. 2024, *ApJ*, 965, 57, doi: [10.3847/1538-4357/ad2705](#)
- Barsdell, B. R., & Jameson, A. 2024, *Heimdall: GPU accelerated transient detection pipeline for radio astronomy*, *Astrophysics Source Code Library*, record ascl:2407.016
- Bassa, C. G., Tendulkar, S. P., Adams, E. A. K., et al. 2017, *ApJL*, 843, L8, doi: [10.3847/2041-8213/aa7a0c](#)
- Behroozi, P. S., Wechsler, R. H., & Conroy, C. 2013, *ApJ*, 770, 57, doi: [10.1088/0004-637X/770/1/57](#)
- Bennett, C. L., Larson, D., Weiland, J. L., & Hinshaw, G. 2014, *ApJ*, 794, 135, doi: [10.1088/0004-637X/794/2/135](#)
- Bettinelli, M., Hidalgo, S. L., Cassisi, S., et al. 2019, *MNRAS*, 487, 5862, doi: [10.1093/mnras/stz1679](#)
- Bhandari, S., Marcote, B., Sridhar, N., et al. 2023, *ApJL*, 958, L19, doi: [10.3847/2041-8213/ad083f](#)
- Bhardwaj, M., Kirichenko, A., & Gil de Paz, A. 2024a, *The Astronomer’s Telegram*, 16613, 1
- Bhardwaj, M., Lee, J., & Ji, K. 2024b, *Nature*, 634, 1065, doi: [10.1038/s41586-024-08065-w](#)
- Bhardwaj, M., Gaensler, B. M., Kaspi, V. M., et al. 2021a, *ApJL*, 910, L18, doi: [10.3847/2041-8213/abeaa6](#)

- Bhardwaj, M., Kirichenko, A. Y., Michilli, D., et al. 2021b, *ApJL*, 919, L24, doi: [10.3847/2041-8213/ac223b](https://doi.org/10.3847/2041-8213/ac223b)
- Bhardwaj, M., Michilli, D., Kirichenko, A. Y., et al. 2024c, *ApJL*, 971, L51, doi: [10.3847/2041-8213/ad64d1](https://doi.org/10.3847/2041-8213/ad64d1)
- Bhusare, Y., Maan, Y., & Kumar, A. 2024, arXiv e-prints, arXiv:2412.13121, doi: [10.48550/arXiv.2412.13121](https://doi.org/10.48550/arXiv.2412.13121)
- Bochenek, C. D., Ravi, V., Belov, K. V., et al. 2020, *Nature*, 587, 59, doi: [10.1038/s41586-020-2872-x](https://doi.org/10.1038/s41586-020-2872-x)
- Bruni, G., Piro, L., Yang, Y. P., et al. 2025, *A&A*, 695, L12, doi: [10.1051/0004-6361/202453233](https://doi.org/10.1051/0004-6361/202453233)
- Cai, J.-H., Li, N., Yang, H.-F., et al. 2025, *A&A*, 694, A271, doi: [10.1051/0004-6361/202452813](https://doi.org/10.1051/0004-6361/202452813)
- Cardelli, J. A., Clayton, G. C., & Mathis, J. S. 1989, *ApJ*, 345, 245, doi: [10.1086/167900](https://doi.org/10.1086/167900)
- Cavaliere, A., & Fusco-Femiano, R. 1976, *A&A*, 49, 137
- Charlot, S., & Fall, S. M. 2000, *ApJ*, 539, 718, doi: [10.1086/309250](https://doi.org/10.1086/309250)
- Chatterjee, S., Law, C. J., Wharton, R. S., et al. 2017, *Nature*, 541, 58, doi: [10.1038/nature20797](https://doi.org/10.1038/nature20797)
- Chen, X.-L., Tsai, C.-W., Li, D., et al. 2025, *ApJL*, 980, L24, doi: [10.3847/2041-8213/adadfd](https://doi.org/10.3847/2041-8213/adadfd)
- CHIME/FRB Collaboration, Andersen, B. C., Bandura, K. M., et al. 2020, *Nature*, 587, 54, doi: [10.1038/s41586-020-2863-y](https://doi.org/10.1038/s41586-020-2863-y)
- CHIME/FRB Collaboration, Andersen, B. C., Bandura, K., et al. 2023, *ApJ*, 947, 83, doi: [10.3847/1538-4357/acc6c1](https://doi.org/10.3847/1538-4357/acc6c1)
- Conroy, C., & Gunn, J. E. 2010, *ApJ*, 712, 833, doi: [10.1088/0004-637X/712/2/833](https://doi.org/10.1088/0004-637X/712/2/833)
- Conroy, C., Gunn, J. E., & White, M. 2009, *ApJ*, 699, 486, doi: [10.1088/0004-637X/699/1/486](https://doi.org/10.1088/0004-637X/699/1/486)
- Cordes, J. M., & Lazio, T. J. W. 2002, arXiv e-prints, astro, doi: [10.48550/arXiv.astro-ph/0207156](https://doi.org/10.48550/arXiv.astro-ph/0207156)
- Cordes, J. M., Ocker, S. K., & Chatterjee, S. 2022, *ApJ*, 931, 88, doi: [10.3847/1538-4357/ac6873](https://doi.org/10.3847/1538-4357/ac6873)
- Dehnen, W., McLaughlin, D. E., & Sachania, J. 2006, *MNRAS*, 369, 1688, doi: [10.1111/j.1365-2966.2006.10404.x](https://doi.org/10.1111/j.1365-2966.2006.10404.x)
- Dutton, A. A., & Macciò, A. V. 2014, *MNRAS*, 441, 3359, doi: [10.1093/mnras/stu742](https://doi.org/10.1093/mnras/stu742)
- Eftekhari, T., Dong, Y., Fong, W., et al. 2025, *ApJL*, 979, L22, doi: [10.3847/2041-8213/ad9de2](https://doi.org/10.3847/2041-8213/ad9de2)
- Fitzpatrick, E. L., & Massa, D. 2007, *ApJ*, 663, 320, doi: [10.1086/518158](https://doi.org/10.1086/518158)
- Foreman-Mackey, D., Sick, J., & Johnson, B. 2014, *Python-Fsps: Python Bindings To Fsps (V0.1.1)*, v0.1.1, Zenodo, doi: [10.5281/zenodo.12157](https://doi.org/10.5281/zenodo.12157)
- Gallazzi, A., Charlot, S., Brinchmann, J., White, S. D. M., & Tremonti, C. A. 2005, *MNRAS*, 362, 41, doi: [10.1111/j.1365-2966.2005.09321.x](https://doi.org/10.1111/j.1365-2966.2005.09321.x)
- Gordon, A. C., Fong, W.-f., Simha, S., et al. 2024, *ApJL*, 963, L34, doi: [10.3847/2041-8213/ad2773](https://doi.org/10.3847/2041-8213/ad2773)
- Greisen, E. W. 2003, in *Astrophysics and Space Science Library*, Vol. 285, *Information Handling in Astronomy - Historical Vistas*, ed. A. Heck, 109, doi: [10.1007/0-306-48080-8_7](https://doi.org/10.1007/0-306-48080-8_7)
- Han, J., Jing, Y. P., Wang, W., Yang, X., & Mo, H. J. 2016, *MNRAS*, 456, 1729, doi: [10.1093/mnras/stv2757](https://doi.org/10.1093/mnras/stv2757)
- Harris, J., & Zaritsky, D. 2009, *AJ*, 138, 1243, doi: [10.1088/0004-6256/138/5/1243](https://doi.org/10.1088/0004-6256/138/5/1243)
- Hewitt, D. M., Bhandari, S., Marcote, B., et al. 2024a, *MNRAS*, 529, 1814, doi: [10.1093/mnras/stae632](https://doi.org/10.1093/mnras/stae632)
- Hewitt, D. M., Bhardwaj, M., Gordon, A. C., et al. 2024b, *ApJL*, 977, L4, doi: [10.3847/2041-8213/ad8ce1](https://doi.org/10.3847/2041-8213/ad8ce1)
- Hsu, T.-Y., Hashimoto, T., Yang, T.-C., et al. 2025, arXiv e-prints, arXiv:2505.03326, doi: [10.48550/arXiv.2505.03326](https://doi.org/10.48550/arXiv.2505.03326)
- Ibata, R. A., McConnachie, A., Cuillandre, J.-C., et al. 2017, *ApJ*, 848, 128, doi: [10.3847/1538-4357/aa855c](https://doi.org/10.3847/1538-4357/aa855c)
- Johnson, B. D., Leja, J., Conroy, C., & Speagle, J. S. 2021, *ApJS*, 254, 22, doi: [10.3847/1538-4365/abef67](https://doi.org/10.3847/1538-4365/abef67)
- Kauffmann, G., Heckman, T. M., Tremonti, C., et al. 2003, *MNRAS*, 346, 1055, doi: [10.1111/j.1365-2966.2003.07154.x](https://doi.org/10.1111/j.1365-2966.2003.07154.x)
- Kaur, B., Kanekar, N., & Prochaska, J. X. 2022, *ApJL*, 925, L20, doi: [10.3847/2041-8213/ac4ca8](https://doi.org/10.3847/2041-8213/ac4ca8)
- Keimpema, A., Kettenis, M. M., Pogrebenko, S. V., et al. 2015, *Experimental Astronomy*, 39, 259, doi: [10.1007/s10686-015-9446-1](https://doi.org/10.1007/s10686-015-9446-1)
- Kennicutt, Jr., R. C. 1998, *ARA&A*, 36, 189, doi: [10.1146/annurev.astro.36.1.189](https://doi.org/10.1146/annurev.astro.36.1.189)
- Kewley, L. J., Dopita, M. A., Sutherland, R. S., Heisler, C. A., & Trevena, J. 2001, *ApJ*, 556, 121, doi: [10.1086/321545](https://doi.org/10.1086/321545)
- Kewley, L. J., Groves, B., Kauffmann, G., & Heckman, T. 2006, *MNRAS*, 372, 961, doi: [10.1111/j.1365-2966.2006.10859.x](https://doi.org/10.1111/j.1365-2966.2006.10859.x)
- Kirsten, F., Snelders, M. P., Jenkins, M., et al. 2021, *Nature Astronomy*, 5, 414, doi: [10.1038/s41550-020-01246-3](https://doi.org/10.1038/s41550-020-01246-3)
- Kirsten, F., Marcote, B., Nimmo, K., et al. 2022, *Nature*, 602, 585, doi: [10.1038/s41586-021-04354-w](https://doi.org/10.1038/s41586-021-04354-w)
- Konijn, D. C., Hewitt, D. M., Hessels, J. W. T., et al. 2024, *MNRAS*, 534, 3331, doi: [10.1093/mnras/stae2296](https://doi.org/10.1093/mnras/stae2296)
- Kovlakas, K., Zezas, A., Andrews, J. J., et al. 2021, *MNRAS*, 506, 1896, doi: [10.1093/mnras/stab1799](https://doi.org/10.1093/mnras/stab1799)
- Kriek, M., & Conroy, C. 2013, *ApJL*, 775, L16, doi: [10.1088/2041-8205/775/1/L16](https://doi.org/10.1088/2041-8205/775/1/L16)
- Kroupa, P. 2001, *MNRAS*, 322, 231, doi: [10.1046/j.1365-8711.2001.04022.x](https://doi.org/10.1046/j.1365-8711.2001.04022.x)

- Kumar, A., Maan, Y., & Bhusare, Y. 2024, *ApJ*, 977, 177, doi: [10.3847/1538-4357/ad84de](https://doi.org/10.3847/1538-4357/ad84de)
- Lee, K.-G., Khrykin, I. S., Simha, S., et al. 2023, *ApJL*, 954, L7, doi: [10.3847/2041-8213/acefb5](https://doi.org/10.3847/2041-8213/acefb5)
- Leja, J., Johnson, B. D., Conroy, C., & van Dokkum, P. 2018, *ApJ*, 854, 62, doi: [10.3847/1538-4357/aaa8db](https://doi.org/10.3847/1538-4357/aaa8db)
- Leja, J., Johnson, B. D., Conroy, C., van Dokkum, P. G., & Byler, N. 2017, *ApJ*, 837, 170, doi: [10.3847/1538-4357/aa5ffe](https://doi.org/10.3847/1538-4357/aa5ffe)
- Lorimer, D. R. 2011, SIGPROC: Pulsar Signal Processing Programs, Astrophysics Source Code Library, record ascl:1107.016. <http://ascl.net/1107.016>
- Lorimer, D. R., Bailes, M., McLaughlin, M. A., Narkevic, D. J., & Crawford, F. 2007, *Science*, 318, 777, doi: [10.1126/science.1147532](https://doi.org/10.1126/science.1147532)
- Loudas, N., Li, D., Strauss, M. A., & Leja, J. 2025, arXiv e-prints, arXiv:2502.15566, doi: [10.48550/arXiv.2502.15566](https://doi.org/10.48550/arXiv.2502.15566)
- Macquart, J. P., Prochaska, J. X., McQuinn, M., et al. 2020, *Nature*, 581, 391, doi: [10.1038/s41586-020-2300-2](https://doi.org/10.1038/s41586-020-2300-2)
- Marcote, B., Paragi, Z., Hessels, J. W. T., et al. 2017, *ApJL*, 834, L8, doi: [10.3847/2041-8213/834/2/L8](https://doi.org/10.3847/2041-8213/834/2/L8)
- Marcote, B., Nimmo, K., Hessels, J. W. T., et al. 2020, *Nature*, 577, 190, doi: [10.1038/s41586-019-1866-z](https://doi.org/10.1038/s41586-019-1866-z)
- Marino, R. A., Rosales-Ortega, F. F., Sánchez, S. F., et al. 2013, *A&A*, 559, A114, doi: [10.1051/0004-6361/201321956](https://doi.org/10.1051/0004-6361/201321956)
- Massana, P., Ruiz-Lara, T., Noël, N. E. D., et al. 2022, *MNRAS*, 513, L40, doi: [10.1093/mnrasl/slac030](https://doi.org/10.1093/mnrasl/slac030)
- Mazzarella, J. M., & NED Team. 2007, NED for a New Era
- McMullin, J. P., Waters, B., Schiebel, D., Young, W., & Golap, K. 2007, in *Astronomical Society of the Pacific Conference Series*, Vol. 376, *Astronomical Data Analysis Software and Systems XVI*, ed. R. A. Shaw, F. Hill, & D. J. Bell, 127
- Mohr, J. J., Mathiesen, B., & Evrard, A. E. 1999, *ApJ*, 517, 627, doi: [10.1086/307624](https://doi.org/10.1086/307624)
- Montes, M., Trujillo, I., Karunakaran, A., et al. 2024, *A&A*, 681, A15, doi: [10.1051/0004-6361/202347667](https://doi.org/10.1051/0004-6361/202347667)
- Moster, B. P., Somerville, R. S., Maulbetsch, C., et al. 2010, *ApJ*, 710, 903, doi: [10.1088/0004-637X/710/2/903](https://doi.org/10.1088/0004-637X/710/2/903)
- Moustakas, J., Scholte, D., Dey, B., & Khederlarian, A. 2023, FastSpecFit: Fast spectral synthesis and emission-line fitting of DESI spectra, Astrophysics Source Code Library, record ascl:2308.005. <http://ascl.net/2308.005>
- Nagao, T., Maiolino, R., & Marconi, A. 2006, *A&A*, 459, 85, doi: [10.1051/0004-6361:20065216](https://doi.org/10.1051/0004-6361:20065216)
- Newville, M., Otten, R., Nelson, A., et al. 2021, lmfit/lmfit-py: 1.0.3, 1.0.3, Zenodo, doi: [10.5281/zenodo.5570790](https://doi.org/10.5281/zenodo.5570790)
- Nimmo, K., Hewitt, D. M., Hessels, J. W. T., et al. 2022, *ApJL*, 927, L3, doi: [10.3847/2041-8213/ac540f](https://doi.org/10.3847/2041-8213/ac540f)
- Niu, C. H., Aggarwal, K., Li, D., et al. 2022, *Nature*, 606, 873, doi: [10.1038/s41586-022-04755-5](https://doi.org/10.1038/s41586-022-04755-5)
- Nugent, A. E., Fong, W.-f., Castrejón, C., et al. 2024, *ApJ*, 962, 5, doi: [10.3847/1538-4357/ad17c0](https://doi.org/10.3847/1538-4357/ad17c0)
- O'Connor, B., Bhardwaj, M., & Palmese, A. 2024, The Astronomer's Telegram, 16426, 1
- Oke, J. B. 1990, *AJ*, 99, 1621, doi: [10.1086/115444](https://doi.org/10.1086/115444)
- Ould-Boukattine, O. S., Chawla, P., Hessels, J. W. T., et al. 2024, arXiv e-prints, arXiv:2410.17024, doi: [10.48550/arXiv.2410.17024](https://doi.org/10.48550/arXiv.2410.17024)
- Ould-Boukattine, O. S., Blaauw, R., Gawronski, M. P., et al. 2025, The Astronomer's Telegram, 16967, 1
- Pasquali, A., Gallazzi, A., & van den Bosch, F. C. 2012, *MNRAS*, 425, 273, doi: [10.1111/j.1365-2966.2012.21454.x](https://doi.org/10.1111/j.1365-2966.2012.21454.x)
- Petroff, E., Hessels, J. W. T., & Lorimer, D. R. 2022, *A&A Rv*, 30, 2, doi: [10.1007/s00159-022-00139-w](https://doi.org/10.1007/s00159-022-00139-w)
- Petrov, L. 2023, *AJ*, 165, 183, doi: [10.3847/1538-3881/acc174](https://doi.org/10.3847/1538-3881/acc174)
- Pillepich, A., Springel, V., Nelson, D., et al. 2018, *MNRAS*, 475, 676, doi: [10.1093/mnras/stx2656](https://doi.org/10.1093/mnras/stx2656)
- Planck Collaboration, Ade, P. A. R., Aghanim, N., et al. 2016, *A&A*, 594, A13, doi: [10.1051/0004-6361/201525830](https://doi.org/10.1051/0004-6361/201525830)
- Prochaska, J. X., & Zheng, Y. 2019, *MNRAS*, 485, 648, doi: [10.1093/mnras/stz261](https://doi.org/10.1093/mnras/stz261)
- Reynolds, R. J. 1977, *ApJ*, 216, 433, doi: [10.1086/155484](https://doi.org/10.1086/155484)
- Salim, S., Rich, R. M., Charlot, S., et al. 2007, *ApJS*, 173, 267, doi: [10.1086/519218](https://doi.org/10.1086/519218)
- Sarazin, C. L. 1986, *X-ray Emission from Clusters of Galaxies* (Cambridge University Press)
- Saulder, C., van Kampen, E., Chilingarian, I. V., Mieske, S., & Zeilinger, W. W. 2016, *A&A*, 596, A14, doi: [10.1051/0004-6361/201526711](https://doi.org/10.1051/0004-6361/201526711)
- Schaller, M., Dalla Vecchia, C., Schaye, J., et al. 2015, *MNRAS*, 454, 2277, doi: [10.1093/mnras/stv1870](https://doi.org/10.1093/mnras/stv1870)
- Schlaflly, E. F., Meisner, A. M., & Green, G. M. 2019, *ApJS*, 240, 30, doi: [10.3847/1538-4365/aafbea](https://doi.org/10.3847/1538-4365/aafbea)
- Seymour, A., Michilli, D., & Pleunis, Z. 2019, DM_phase: Algorithm for correcting dispersion of radio signals, Astrophysics Source Code Library, record ascl:1910.004. <http://ascl.net/1910.004>
- Shah, V., Shin, K., Leung, C., et al. 2025, *ApJL*, 979, L21, doi: [10.3847/2041-8213/ad9ddc](https://doi.org/10.3847/2041-8213/ad9ddc)
- Sharma, K., Ravi, V., Connor, L., et al. 2024, *Nature*, 635, 61, doi: [10.1038/s41586-024-08074-9](https://doi.org/10.1038/s41586-024-08074-9)

- Shepherd, M. C. 1997, in *Astronomical Society of the Pacific Conference Series*, Vol. 125, *Astronomical Data Analysis Software and Systems VI*, ed. G. Hunt & H. Payne, 77
- Shin, K., & CHIME/FRB Collaboration. 2024, *The Astronomer's Telegram*, 16420, 1
- Shin, K., Curtin, A., Fine, M., et al. 2025, arXiv e-prints, arXiv:2505.13297, doi: [10.48550/arXiv.2505.13297](https://doi.org/10.48550/arXiv.2505.13297)
- Simha, S., Lee, K.-G., Prochaska, J. X., et al. 2023, *ApJ*, 954, 71, doi: [10.3847/1538-4357/ace324](https://doi.org/10.3847/1538-4357/ace324)
- Snelders, M. P., Bhandari, S., Kirsten, F., et al. 2024, *The Astronomer's Telegram*, 16542, 1
- Somerville, R. S., Behroozi, P., Pandya, V., et al. 2018, *MNRAS*, 473, 2714, doi: [10.1093/mnras/stx2040](https://doi.org/10.1093/mnras/stx2040)
- Spitler, L. G., Scholz, P., Hessels, J. W. T., et al. 2016, *Nature*, 531, 202, doi: [10.1038/nature17168](https://doi.org/10.1038/nature17168)
- Springel, V., Wang, J., Vogelsberger, M., et al. 2008, *MNRAS*, 391, 1685, doi: [10.1111/j.1365-2966.2008.14066.x](https://doi.org/10.1111/j.1365-2966.2008.14066.x)
- Taylor, E. N., Hopkins, A. M., Baldry, I. K., et al. 2011, *MNRAS*, 418, 1587, doi: [10.1111/j.1365-2966.2011.19536.x](https://doi.org/10.1111/j.1365-2966.2011.19536.x)
- Tendulkar, S. P., Bassa, C. G., Cordes, J. M., et al. 2017, *ApJL*, 834, L7, doi: [10.3847/2041-8213/834/2/L7](https://doi.org/10.3847/2041-8213/834/2/L7)
- Tendulkar, S. P., Gil de Paz, A., Kirichenko, A. Y., et al. 2021, *ApJL*, 908, L12, doi: [10.3847/2041-8213/abdb38](https://doi.org/10.3847/2041-8213/abdb38)
- Tian, J., Pastor-Marazuela, I., Stappers, B., et al. 2024a, *The Astronomer's Telegram*, 16446, 1
- Tian, J., Rajwade, K. M., Pastor-Marazuela, I., et al. 2024b, *MNRAS*, 533, 3174, doi: [10.1093/mnras/stae2013](https://doi.org/10.1093/mnras/stae2013)
- van Straten, W., & Bailes, M. 2011, *PASA*, 28, 1, doi: [10.1071/AS10021](https://doi.org/10.1071/AS10021)
- Vikhlinin, A., Kravtsov, A., Forman, W., et al. 2006, *ApJ*, 640, 691, doi: [10.1086/503355](https://doi.org/10.1086/503355)
- Weisz, D. R., Dolphin, A. E., Skillman, E. D., et al. 2015, *ApJ*, 804, 136, doi: [10.1088/0004-637X/804/2/136](https://doi.org/10.1088/0004-637X/804/2/136)
- Wen, Z. L., & Han, J. L. 2024, *DESI Legacy Imaging Survey*
- Wen, Z. L., & Han, J. L. 2024, *ApJS*, 272, 39, doi: [10.3847/1538-4365/ad409d](https://doi.org/10.3847/1538-4365/ad409d)
- Wetzel, A. R., Tollerud, E. J., & Weisz, D. R. 2014, *MNRAS*, 439, 1161, doi: [10.1093/mnras/stt2435](https://doi.org/10.1093/mnras/stt2435)
- Whitney, A., Kettenis, M., Phillips, C., & Sekido, M. 2010, in *Sixth International VLBI Service for Geodesy and Astronomy. Proceedings from the 2010 General Meeting*, ed. R. Navarro, S. Rogstad, C. E. Goodhart, E. Sigman, M. Soriano, D. Wang, L. A. White, & C. S. Jacobs, 192–196
- Xie, J.-T., Feng, Y., Li, D., et al. 2024, arXiv e-prints, arXiv:2410.10172, doi: [10.48550/arXiv.2410.10172](https://doi.org/10.48550/arXiv.2410.10172)
- Xu, H., Niu, J. R., Chen, P., et al. 2022, *Nature*, 609, 685, doi: [10.1038/s41586-022-05071-8](https://doi.org/10.1038/s41586-022-05071-8)
- Yamasaki, S., & Totani, T. 2020, *The Astrophysical Journal*, 888, 105
- Yao, J. M., Manchester, R. N., & Wang, N. 2017, *ApJ*, 835, 29, doi: [10.3847/1538-4357/835/1/29](https://doi.org/10.3847/1538-4357/835/1/29)
- Zhang, B. 2020, *Nature*, 587, 45, doi: [10.1038/s41586-020-2828-1](https://doi.org/10.1038/s41586-020-2828-1)
- Zhang, J., Wu, Q., Cao, S., et al. 2024, *The Astronomer's Telegram*, 16505, 1
- Zhang, X., & Yu, W. 2024, *The Astronomer's Telegram*, 16695, 1
- Zou, H., Gao, J., Zhou, X., & Kong, X. 2019, *ApJS*, 242, 8, doi: [10.3847/1538-4365/ab1847](https://doi.org/10.3847/1538-4365/ab1847)